Light and stable triplet bipolarons on square and triangular lattices

J.P. Hague

Department of Physics and Astronomy, The Open University, Walton Hall, Milton Keynes, MK7 6AA, UK

P.E. Kornilovitch

Hewlett-Packard Company, 1000 NE Circle Blvd, Corvallis, Oregon 97330, USA

(Dated: 7th October 2009)

We compute the properties of singlet and triplet bipolarons on two-dimensional lattices using the continuous time quantum Monte Carlo algorithm. Properties of the bipolaron including the total energy, inverse mass, bipolaron radius and number of phonons associated with the bipolaron demonstrate the qualitative difference between models of electron phonon interaction with long-range interaction (screened Fröhlich) and those with purely local (Holstein) interaction. A major result of our survey of the parameter space is the existence of extra-light hybrid singlet bipolarons consisting of an on-site and an off-site component on both square and triangular lattices. We also compute triplet properties of the bipolarons and the pair dispersion. For pair momenta on the edge of the Brillouin zone of the triangular lattice, we find that triplet states are more stable than singlets.

I. INTRODUCTION

Layered superconductors such as the cuprates[1], iron pnictides[2] and others such as hydrated cobaltates ($Na_x CoO_2 \cdot 1.3H_2O$) (Ref. 3) have the potential to completely change thinking about the origins of superconductivity. Given the importance of such a re-think, a number of competing theories and mechanisms have been suggested, which aim to understand superconductivity in layered materials on at least a qualitative level[4,5,6,7,8,9,10,11]. For example, it has been suggested that one way of explaining high temperature superconductivity in cuprates is the condensation of pre-formed bipolarons[7]. A complete quantitative understanding of bipolaron formation, especially in the intermediate coupling regime is needed to judge the applicability of such a theory, especially when the electron-phonon interaction is not perfectly local (i.e. when the Holstein interaction is not appropriate) as is to be expected in real materials.

There are a number of exact numerical methods for studying bipolaron formation in one-dimensional (1D) systems with electron-phonon interactions such as exact diagonalization (ED)[12,13], advanced variational techniques[14], density matrix renormalization group (DMRG)[15] and various quantum Monte-Carlo (QMC) approaches[16,17,18]. In two-dimensional (2D) systems, many of those techniques are not applicable. Exact diagonalization cannot cope with large numbers of lattice sites, DMRG schemes are not easy to develop in 2D and both ED and DMRG can suffer from a truncation of the phonon Hilbert space, rendering those methods inefficient at strong electron-phonon coupling. Also, advanced variational techniques are not easily generalized to 2D. On the other hand, QMC techniques (and especially continuous time QMC) can cope with large lattice sizes and treat the phonon degrees of freedom exactly, making them well suited for computations of bipolarons

on two- and potentially even three- dimensional lattices.

There is a fascinating possibility relating to bipolarons in 2D. If a lattice is made up from triangular plaquettes, and if there is a strong Coulomb repulsion keeping bipolarons from pairing on-site, superlight small bipolarons can form[19,20,21,22]. Our aim here is to comprehensively compute the properties of bipolarons with long range interaction on both square and triangular lattices to determine if there are any other promising ways that bipolarons can pair. The Hubbard-Holstein bipolaron on the square lattice was studied by Macridin *et al.* using the related diagrammatic quantum Monte Carlo technique (DMC)[23]. Our current study goes beyond this previous work by computing the properties of bipolarons formed from long range electron-phonon interactions. We also compute properties of bipolarons on triangular lattices, which have not been comprehensively studied even for the Holstein interaction. Our continuous-time quantum Monte Carlo (CTQMC) algorithm is particularly efficient for this task, since phonon degrees of freedom can be treated exactly to generate an effective retarded interaction between electrons.

In this article, we study the screened Hubbard-Fröhlich model, which has the Hamiltonian,

$$H = -t \sum_{\langle nn' \rangle \sigma} c^\dagger_{n'\sigma} c_{n\sigma} + U \sum_n c^\dagger_{n\uparrow} c_{n\uparrow} c^\dagger_{n\downarrow} c_{n\downarrow} \quad (1)$$

$$+ \sum_m \frac{\hat{P}^2_m}{2M} + \sum_m \frac{\xi^2_m M\omega^2}{2} - \sum_{nm\sigma} f_m(n) c^\dagger_{n\sigma} c_{n\sigma} \xi_m \,.$$

Here, $c^\dagger_n$ creates an electron on site n, t is the inter-site hopping integral, U is the Hubbard repulsion, M is the ion mass, ω the ion oscillation frequency, ζ the ion displacement and $\hat{P}$ the ion momentum. The electron-ion force function is f, and has the form $f_m(n) = \kappa \left[(m-n)^2 + 1 \right]^{-3/2} \exp\left(-|m-n|/R_{sc}\right)$. The screening radius R_{sc} controls the length of the interaction, and

κ is the strength of the interaction. $\boldsymbol{m}$ represents the position of the ion and $\boldsymbol{n}$ is the position of the electron. The electron-ion interaction leads to an effective retarded electron-electron interaction characterized by the function,

$$\Phi_{\Delta\boldsymbol{r}}(\boldsymbol{r}(\tau),\boldsymbol{r}(\tau')) = \sum_{\boldsymbol{m}} f_{\boldsymbol{m}}[\boldsymbol{r}(\tau)]f_{\boldsymbol{m}+\Delta\boldsymbol{r}}[\boldsymbol{r}(\tau')] \qquad (2)$$

where $\Delta\boldsymbol{r}$ is the offset between end configurations of the paths. By changing R_{sc} it is possible to investigate the Hubbard-Holstein model ($R_{sc} \to 0$) and the Hubbard-Fröhlich model ($R_{sc} \to \infty$). We also consider a model similar to the nearest-neighbor model of Bonča and Trugman[24], where effective electron-electron interactions are truncated at near-neighbor sites ($\Phi(\boldsymbol{a}) = \Phi(0)/2$ and all other $\Phi = 0$ where $\boldsymbol{a}$ are vectors to the near-neighbor sites). This simplified model maps directly onto a $U-V$ model in the large phonon frequency limit, and could be particularly useful for understanding limiting behavior[37].

This article is structured as follows. In section II, we briefly review the differences between the CTQMC algorithm in 1D and 2D. In sections III and IV we make a comprehensive survey of the parameter space of singlet bipolarons in 2D. Triplet properties are discussed in section V. One of the additional advantages of our algorithm is that bipolaron dispersions can be computed efficiently, especially in the large λ regime, and these are shown in section VI. Finally we summarize in section VII.

II. METHOD

We use a continuous time quantum Monte Carlo algorithm based on path integrals. We have previously discussed our algorithm in detail with regard to computations in 1D[16], so we do not repeat those details here. There are a few small subtleties relating to using the algorithm in 2D, especially on a triangular lattice, which are discussed here. Our algorithm has been thoroughly checked against results from the U-V model.

A. Triple kink insertions on triangular lattices

There is a subtle difference to the algorithm on triangular lattices, or more generally on any lattice where an electron can return to its original position in 3 hops (such as lattices with nearest and next-nearest neighbor hopping). We illustrate this by considering an example configuration that is permitted on such lattices: Let one of the paths have no kinks and the other path have 3 kinks - one in each of the nearest neighbor directions - so that the start and end of each path lies on the same lattice site. Such a configuration is clearly permitted, since the periodic boundary conditions in imaginary time are satisfied. However, if only binary kink insertions are included in the algorithm then it is not possible to update between configurations with odd and even numbers of

kinks. Thus, to ensure ergodicity, an update with a 3 kink insertion is proposed.

Our scheme for 3 kink insertion is similar to the one that we use for binary updates. To avoid complications, we do not weight the positions of the kinks in imaginary time. Ternary kink insertions do not need to be especially efficient; if path configurations can be updated from even to odd numbers of kinks (and vice-versa) with reasonable regularity, binary insertions can be used to sample the remaining configurations efficiently. Our scheme is as follows,

1. We select a kink type from the 6 possible kinks and assign the label $\boldsymbol{l}_1$.

2. We choose kinks at 120° and 240° rotations from $\boldsymbol{l}_1$ and assign them the labels $\boldsymbol{l}_2$ and $\boldsymbol{l}_3$

3. We choose insertion or removal of kinks with equal probability $1/2$.

4. If inserting, we choose imaginary times τ_1, τ_2 and τ_3 for the new kinks with equal probability $1/\beta$ from the interval $[1,\beta)$.

5. If removal is selected and there is not at least one of each type of kink, then abort. Otherwise select a kink of type $\boldsymbol{l}_1$ for removal with equal probability $1/N_{\boldsymbol{l}_1}$, etc

If configuration $[D]$ has three more kinks than configuration $[C]$, then insertion takes place with probability

$$P[C \to D] = \min\left\{\frac{(t\beta)^3}{N_{\boldsymbol{l}_1}[D]N_{\boldsymbol{l}_2}[D]N_{\boldsymbol{l}_3}[D]}e^{A[C]-A[D]},1\right\} \tag{3}$$

and for removal,

$$P[D \to C] = \min\left\{\frac{N_{\boldsymbol{l}_1}[D]N_{\boldsymbol{l}_2}[D]N_{\boldsymbol{l}_3}[D]}{(t\beta)^3}e^{A[D]-A[C]},1\right\} \tag{4}$$

Note that the number $N_{\boldsymbol{l}_1}[D]$ represents the number of kinks of type $\boldsymbol{l}_1$ in configuration D. Therefore when kinks are inserted, this is the number of kinks in the final configuration. When kinks are removed, $N_{\boldsymbol{l}_1}[D]$ is the number of kinks in the initial configuration.

B. Path exchange in 2D

There is a small difference between exchange in 1D and 2D, especially on the triangular lattice. In 1D, exchange can be carried out by inserting and removing kinks and antikinks. The form of the exchange update in 1D is,

$$P(C \to D) = \min\{1, Q_{\boldsymbol{l},-\boldsymbol{l}}^{(A)}Q_{-\boldsymbol{l},\boldsymbol{l}}^{(B)}\exp(A[C] - A[D])\} \tag{5}$$

where,

$$Q_{\boldsymbol{l},-\boldsymbol{l}}^{(A)} = (t\beta)^{2n_A-\Delta}\frac{\min(N_{A-\boldsymbol{l}},\Delta)+1}{\min(N_{A\boldsymbol{l}}+n_A,\Delta)+1}\frac{N_{A-\boldsymbol{l}}P_{\Delta-n_A}}{N_{A\boldsymbol{l}+n_A}P_{n_A}} \tag{6}$$

here Δ is the displacement between the $\tau = \beta$ ends of path A and path B. $_nP_k = n!/(n-k)!$ is the number of permutations. There are $N_p = \min(N_{A-\boldsymbol{l}}, \Delta) + 1$ possible updates that can be made by inserting n_A kinks into path A and removing m_A antikinks, where $n_A + m_A = \Delta$. m_A is chosen with equal weighting $1/N_p$. $N_{A\boldsymbol{l}}$ is the number of kinks of type $\boldsymbol{l}$ on path A. The expression for path B is similar, but the kink and anti-kink assignments are reversed to get displacement $-\Delta$.

In 2D, two sets of kinks and antikinks in different directions are required to exchange the ends of the paths, so the exchange update has the form,

$$P(C \to D) = \min\{1, \exp(A[C] - A[D]) \prod_{i=1}^{d} Q_{\boldsymbol{l}_i, -\boldsymbol{l}_i}^{(A)} Q_{-\boldsymbol{l}_i, \boldsymbol{l}_i}^{(B)}\}$$
(7)

where there is a different Δ for each kink type to be inserted (and thus a different N_p and m which should be chosen independently for each kink type and path) as determined from the number of kinks that would be required to hop from the end of one path to the end of the other. d is the number of lattice dimensions.

For the triangular lattice, the choice of the two kink directions is not unique, since the kinks are not orthogonal. There are six nearest neighbor vectors representing kinks. To carry out the update, kinks representing two different directions are chosen with equal weight from all available possibilities (that is the two chosen kinks may not be antikinks of each other). Since an equal weight scheme is used, the factors relating to the probability of this choice cancel on both sides of the balance equations. It is important to choose kinks from all possible directions to improve the efficiency of the algorithm.

C. Global path shifts

As in the 1D case, a useful update displaces a single path when the configurations are not exchanged. In both cases, one of the paths is chosen with equal probability, a kink direction is chosen with equal probability and then the path is shifted through r lattice sites, where r is an integer chosen randomly between 0 and $R_{\max} - 1$. Typically $R_{\max} = 50$ for lattice size 100. Failure to include global path shifts leads to an inefficient algorithm with large correlation between measurement, which is especially bad when the bipolaron is only just bound. Global shifts are essential when the bipolaron radius is to be measured.

III. SINGLETS ON THE SQUARE LATTICE

The survey of the bipolaron parameter space begins by considering singlet properties of bipolarons on the square lattice. We will examine the effects of the electron-phonon coupling, Hubbard repulsion and inter-action range on the bipolarons. In the following, we take $\bar{\omega} = \omega/t = 1$, which corresponds to $\omega/W = 1/4$ which is well inside the adiabatic regime. W is the half band width or energy of a single non-interacting electron. $W = 4t$ for the square lattice and $W = 6t$ for the triangular lattice. We restrict paths to lie within 100 lattice spacings of each other, with the large lattice size used to ensure that the effects of the lattice restriction are minimal (this should be true where the bipolaron radius is much smaller than the lattice size). Most properties are not strongly affected by finite size effects. We note that the inverse radius is the most sensitive measurement, and the total energy the least sensitive. The most severe finite size effect is that premature binding can occur if the paths are too closely restricted.

Figure 1 shows the total energy of the two polarons / bipolaron pair for a range of electron-phonon coupling strengths, interaction screening radius and Hubbard U. As is the case in 1D[16], a qualitative difference can be seen between bipolarons formed with Holstein and screened Fröhlich interactions. At large U, the energy curves for the Hubbard-Holstein bipolaron are flat, indicating that the bipolaron has unbound into two polarons. This is true for all the λ shown, indicating that there is no bound singlet bipolaron in the $U \to \infty$ Hubbard-Holstein model. The significance for triplet states will be discussed later in the article.

In contrast to the flat energy curves characterizing the large U, large λ Holstein model, the energy of the Hubbard-Fröhlich bipolaron changes on varying U, indicating that there are bound singlet states even for very large U (we will revisit this point later in the article). For small λ and $R_{sc} \neq 0$, the energy curves are flat at large U. The model with only nearest-neighbor interaction ($\Phi(\boldsymbol{a}) = 0.5$) has similar properties to the $R_{sc} = 2$ and $R_{sc} = 3$ models. $\Phi(\boldsymbol{a}) = 0.438$ to 3 significant figures for the model with $R_{sc} = 2$ and $\Phi(\boldsymbol{a}) = 0.509$ to 3 significant figures for the model with $R_{sc} = 3$, indicating that bipolaron properties depend most strongly on the nearest neighbor part of the Fröhlich interaction, rather than the tails.

Is is useful to quickly describe the limiting behaviors of the bipolarons. First, it is appropriate to introduce some notation. We use S0 to define a strongly bound on-site singlet pair where the two electrons are separated by no lattice spacings and use S1 to denote a strongly bound inter-site pair where the electrons are separated by one lattice space[23]. As discussed for the 1D model[16], if bipolarons are strongly bound the renormalized inter-site hopping is small, and an atomic Hamiltonian can be determined using the Lang–Firsov transformation:

$$\tilde{H}_{\text{at}} = -\sum_{\boldsymbol{n}\boldsymbol{n}'} \frac{W\lambda\Phi_0(\boldsymbol{n}, \boldsymbol{n}')}{\Phi_0(0,0)} \hat{n}_{\boldsymbol{n}} \hat{n}_{\boldsymbol{n}'} + \omega \sum_{\boldsymbol{m}} \left(d_{\boldsymbol{m}}^{\dagger} d_{\boldsymbol{m}} + \frac{1}{2} \right)$$
(8)

Since the electron number operator, $\hat{n}$ is unchanged under the Lang–Firsov transformation, the effects of the Hubbard U can quickly be reintroduced. Thus, for a
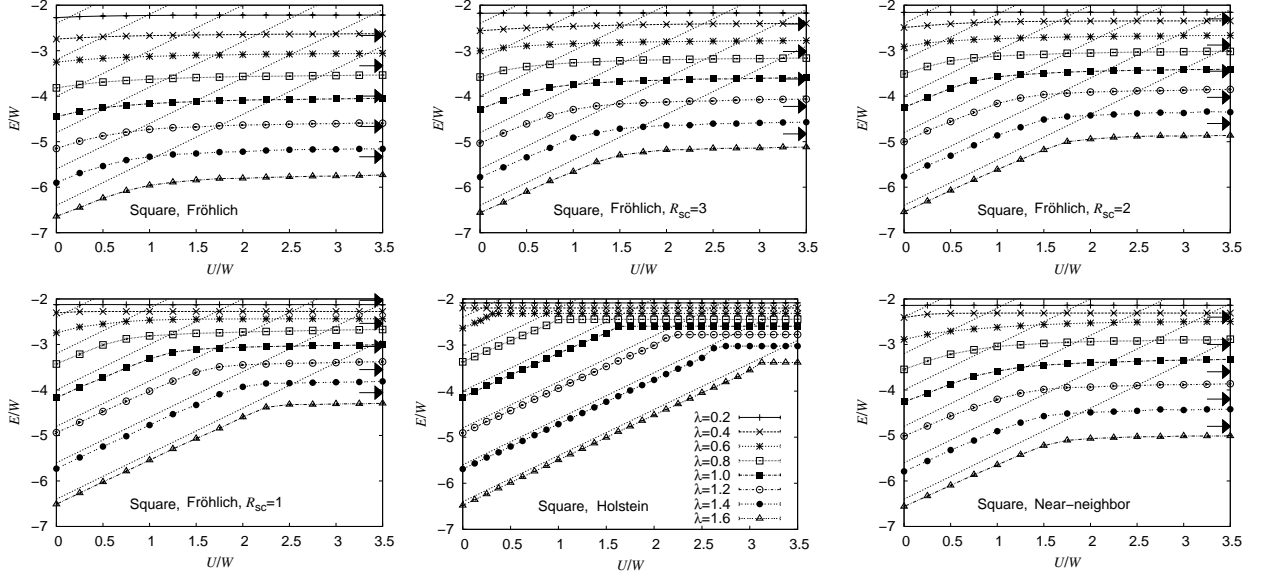
FIG. 1: Total energy of bipolarons on the square lattice for various U, λ, R_{sc}, $\bar{\omega} = 1$ and $\bar{\beta} = \beta/t = 14$. There is a clear qualitative difference between bipolarons with long range interactions and those formed from the purely local Holstein interaction. Unless otherwise indicated, error bars represent three standard deviations. Where error bars are not visible, they are smaller than the points.
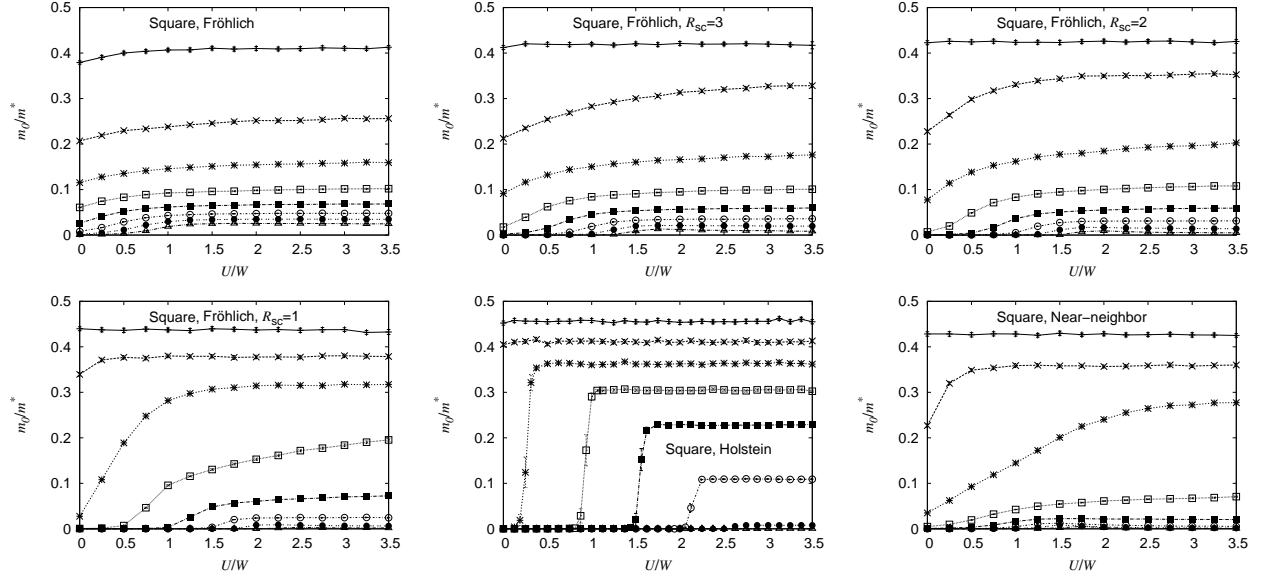

FIG. 2: Inverse mass of bipolarons on the square lattice. Parameters are the same as in Fig. 1. Again, qualitative differences between the bipolarons formed via the purely site local Holstein interaction and the long-range interactions can be seen.

strongly bound onsite (S0) bipolaron,

$$E = U - 4W\lambda \qquad (9)$$

W is the non-interacting kinetic energy of a single particle (half band-width). The limiting behavior of the S0 bipolaron is shown on the plots as dashed lines. As in the 1D case, the S0 Hubbard-Holstein bipolaron rapidly becomes strongly bound on decreasing U. For the longer range interactions, it takes much more attraction to strongly bind the S0 bipolaron. We can also compute the

energy of the strongly bound S1 bipolaron which forms at large λ and $U \gg W\lambda$,

$$E = -2W\lambda[1 + \Phi(\boldsymbol{a})/\Phi_0]. \qquad (10)$$

The energy of the strongly bound S1 state is plotted in Fig. 1 as the arrows at $U/W = 3.5$ (note that only 5 arrows corresponding to the largest λ are shown). The energy of the strongly bound S1 bipolaron is higher than the simulated energy, but the values converge as λ increases. From the difference in energies between the S1
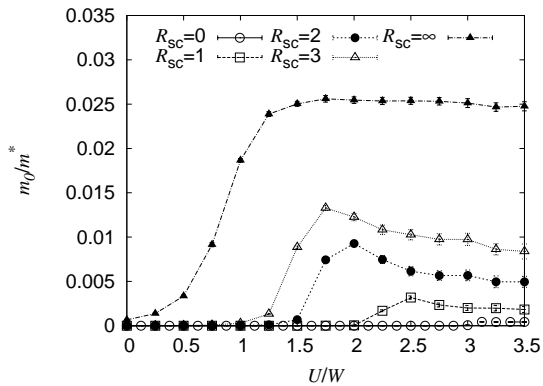
FIG. 3: Comparison of the inverse mass for bipolarons on the square lattice. $\lambda = 1.6$ and various interaction ranges are considered. Other parameters are as in Fig. 1. At intermediate U, the energies of the on-site (S0) and intersite (S1) bipolarons are degenerate, so a light bipolaron can be formed without the need for triangular plaquettes.

limit and the simulated energy, it appears that the bipolarons formed from heavily screened interactions have a stronger S1 character.

The inverse mass of the bipolarons is shown in Fig. 2. Again, significant differences between Hubbard-Holstein and Hubbard-Fröhlich bipolarons can immediately be seen. In the Hubbard-Holstein model, the mass changes very rapidly with U when the bipolaron binds, with a mass change of several orders of magnitude over a very small range of U values. This rapid change is not seen for the Fröhlich bipolaron, which maintains a similar mass over a wide range of U. For the larger λ values and large U, the system of two particles appears to be heavier in the Fröhlich case. This is because the Holstein bipolaron is not bound for those values, whereas the Frölich interaction leads to an intersite (S1) bipolaron.

In comparison to the U dependence of the mass of the 1D Holstein bipolaron, which can be found in Ref. 16, the change in mass with U is extremely rapid on the square lattice. In contrast, the mass relating to long range interactions is qualitatively unchanged, with the formation of a relatively light bipolaron (even in comparison with a free electron) over a very wide range of the parameter space. The qualitative difference between the properties of Holstein and Fröhlich bipolarons emphasizes that while the Holstein model may be a reasonable approximation for considering polarons in organic molecular compounds, the simple Holstein approximation is inappropriate for many crystalline systems where complete screening of the electron-phonon interaction is not possible. Even if the screening length is as small as a single lattice spacing, bipolarons have significantly modified properties compared with those formed in the Holstein model.

In 1D, a crab like bipolaron can form in models with long range interaction when the energies of on-site and off-site configurations are degenerate (S1 like configura-

tions can be changed to S0 with a single hop, without any energy barrier to make the process second order in t). This leads to a noticeable decrease in mass at intermediate U. It is of interest to determine if these lighter bipolarons can also form on the square lattice. In Fig. 3, the masses of bipolarons formed when $\lambda = 1.6$ are examined as R_{sc} is changed. A peak in the inverse mass (decrease in the mass) is clearly visible at intermediate U and is especially pronounced when $R_{sc} = 2$. Comparing equations 9 and 10, it can be seen that for large phonon frequencies, the peak would be expected at $U/W = 2\lambda[1-\Phi(\boldsymbol{a})/\Phi(0)]$, which corresponds to $U/W = 1.798$ for $R_{sc} = 2$ (to 4 s.f) in good agreement. The presence of this peak shows that light bipolarons can exist on square lattices without the need for triangular plaquettes. Naturally, such a state depends on a very subtle balance of parameters and could not be realized in all crystalline systems.

As in the case of the 1D bipolaron, analytical determination of the effective mass, even for limiting values of the parameters, is difficult (and may not be possible) when there are long range tails in the interaction. While we have not computed limiting behaviors of the mass for the model with only near-neighbor interaction, we expect that a similar approach to that applied to the 1D bipolaron by Bonča and Trugman could yield results[25].

We also show the number of phonons associated with the bipolaron cloud (Fig. 4). As before, the properties of the Hubbard-Holstein bipolaron are qualitatively different to the bipolarons formed from long-range electron phonon interaction. The number of phonons associated with the Holstein bipolaron shows an abrupt increase as the bipolaron binds on decreasing U, whereas there is a smoother crossover from S1 to S0 behavior associated with the screened Fröhlich interaction.

The total number of phonons associated with the strongly bound onsite bipolaron (following the argument in Ref. 21) is,

$$N_{\mathrm{ph}} = \frac{4W\lambda}{\omega}. \qquad (11)$$

This number is independent of U, so the number of phonons reaches a limiting value on decreasing U as seen in Fig. 4 (the strongly bound S0 limit is represented by arrows on the left of the graph). The Holstein bipolaron with large λ quickly reaches the S0 limit at low U. Bipolarons formed with long range interactions approach the S0 limit less rapidly since the longer range tails lead to a shallower effective potential.

The number of phonons associated with the S1 bipolaron can also be found,

$$N_{\mathrm{ph}} = \frac{2W\lambda}{\omega}\left[1 + \frac{\Phi(\boldsymbol{a})}{\Phi_0}\right]. \qquad (12)$$

This is represented as arrows on the large U side of the plots. The agreement improves on increasing λ. Again, it is clear that the most heavily screened interactions have the most clearly defined S1 character.
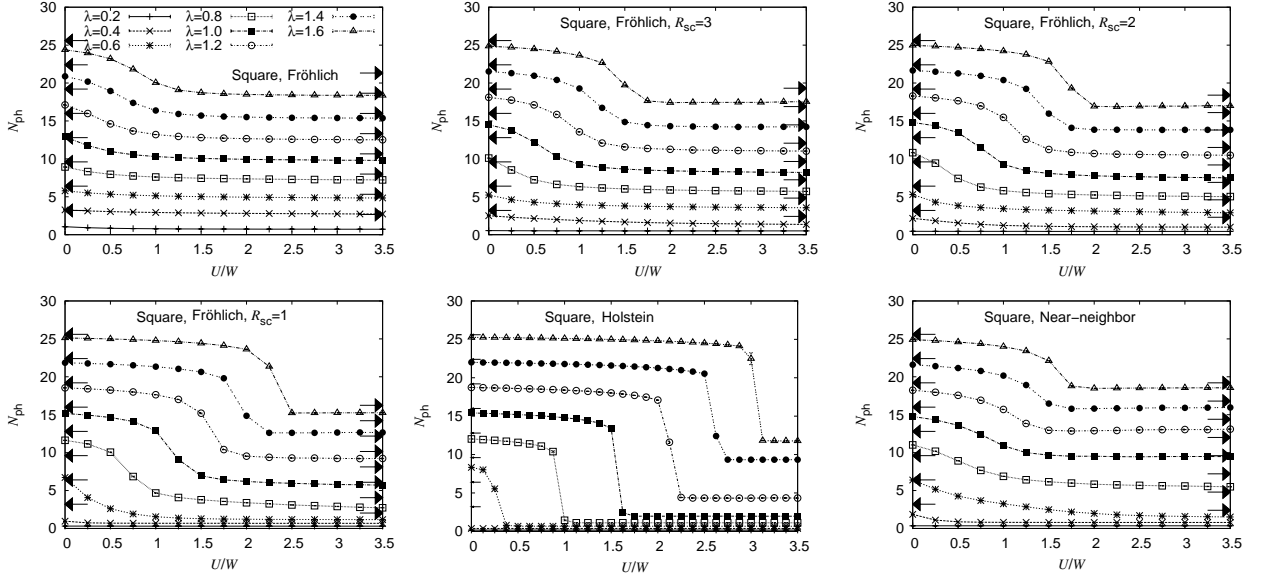
FIG. 4: Number of phonons associated with bipolarons on the square lattice. Parameters are identical to Fig. 1. Again, the properties of the Holstein bipolaron are qualitatively different to those of the Fröhlich bipolaron.
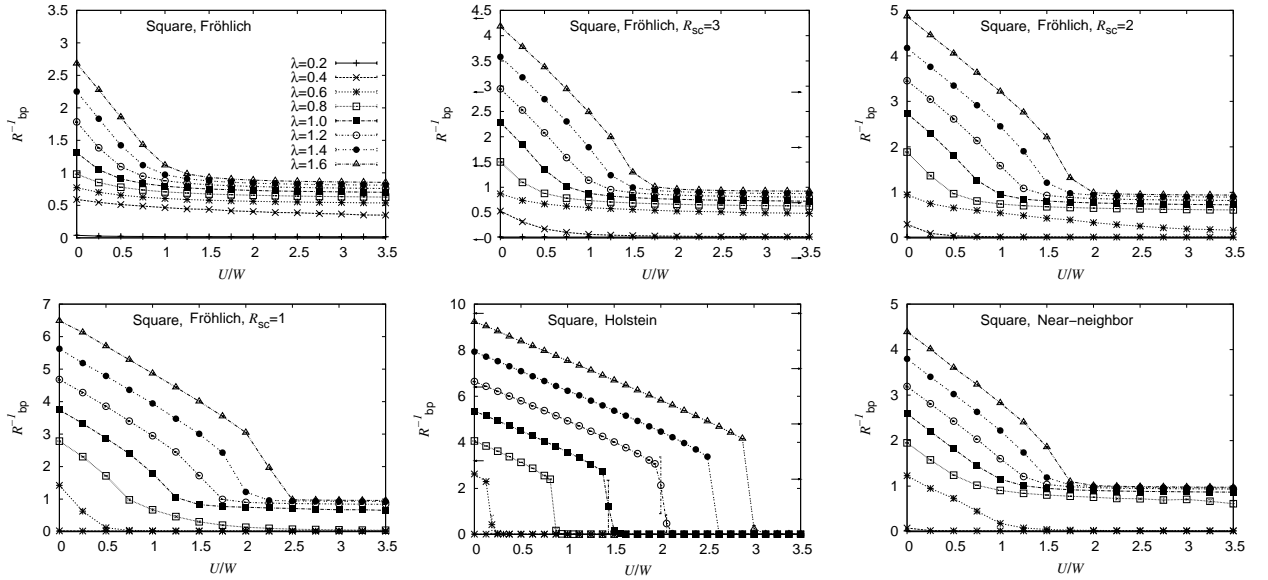

FIG. 5: Inverse bipolaron size associated with bipolarons on the square lattice. Parameters as in Fig. 1.

We complete this section by examining the inverse bipolaron size associated with the square lattice. Again, qualitative differences exist between the Holstein bipolaron and the Fröhlich bipolarons, with S1 bipolarons forming in the screened Fröhlich model at large U and λ indicated by a radius of around a lattice spacing. Comparison with figure 2 shows that bipolarons on the square lattice with long range interaction may be both small and light at intermediate and large λ and intermediate U, where polarons are bound into the hybrid S0-S1 bipolaron.

IV. SINGLETS ON THE TRIANGULAR LATTICE

In this section, attention is turned to the properties of bipolarons on the triangular lattice, which have already been shown to have unusual properties[21]. To ensure that results for bipolarons on square and triangular lattices can be meaningfully compared, we have kept energy scales fixed in terms of W (the non-interacting kinetic energy of a single particle) rather than t. For the square lattice, $W = 4t$, while for the triangular lattice, $W = 6t$. Similar considerations should be made when
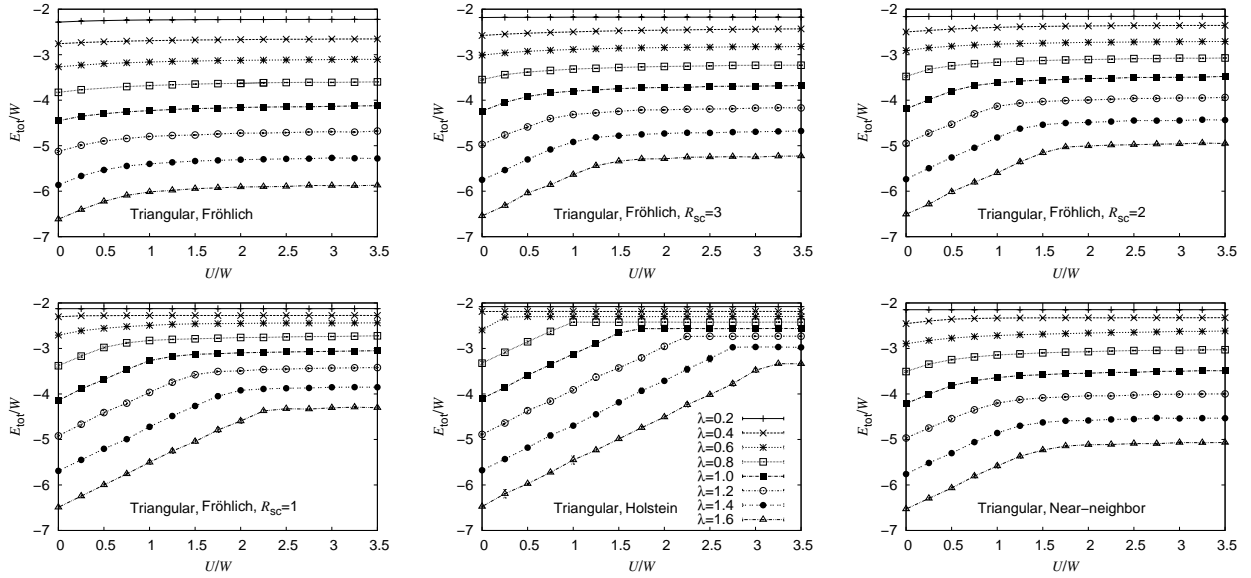
FIG. 6: Total energy of singlet bipolarons on the triangular lattice. $\omega/t = 1.5$, U, λ and R_{sc} are varied, $\bar{\beta} = 28/3$. The value of ω/t is chosen so that ω/W is the same for both square and triangular lattices. The energies are qualitatively similar to those associated with the square lattice.
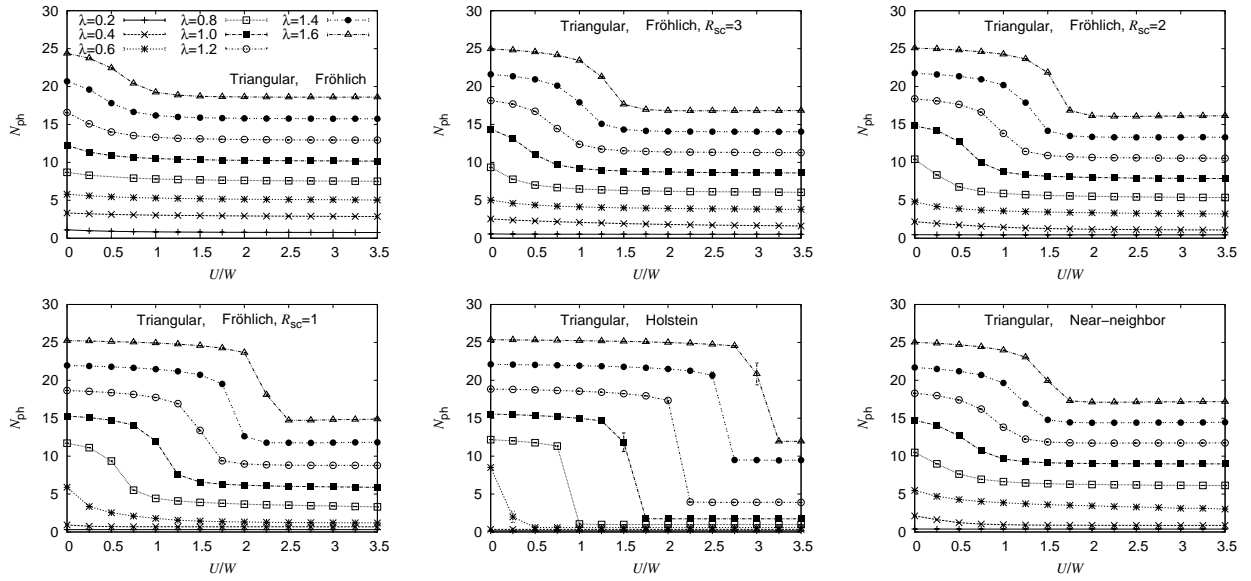

FIG. 7: Number of phonons associated with bipolarons on the triangular lattice. Parameters are as in Fig. 6.

comparing plots of total energy between lattice types, which is why we have quoted all energy scales in these sections in terms of W. Also, to keep the ratio $\omega/W = 1/4$, all properties in this section are computed for $\omega/t = 1.5$. Finally, for the same reason, the temperature is also 3/2 higher than that used for computations of the bipolaron on the square lattice, so $\bar{\beta} = 28/3$.

Figure 6 shows the total energy of bipolarons on the triangular lattice as U, λ and R_{sc} are changed. A quick inspection indicated that there is no clear qualitative difference between the total energy of bipolarons on square

and triangular lattices. The same is true of the number of phonons associated with the bipolaron, which is shown in Fig. 7. It is quite surprising that the properties are so similar, since there are very different hopping mechanisms on the triangular lattice compared to the square lattice (such as the possibility for S1 bipolarons to move with a single hop on the triangular lattice, while intersite bipolarons on the square lattice have to tunnel through a high energy intermediate state to move). However, careful comparison shows that in the strong U limit (where inter-site S1 bipolarons are formed)
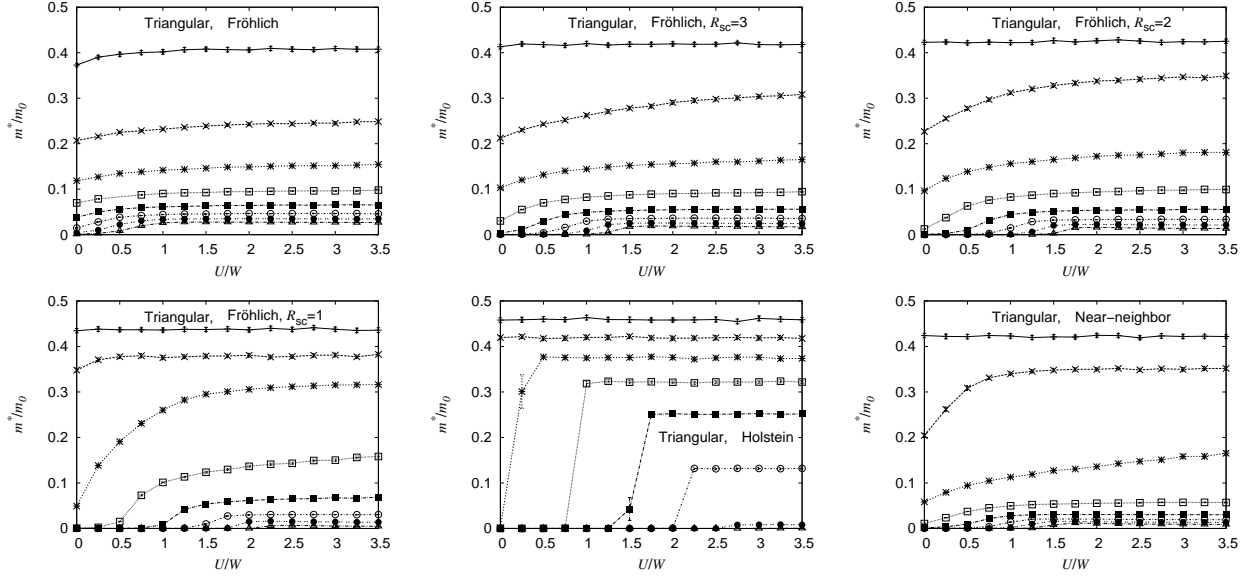
FIG. 8: Inverse mass of bipolarons on the triangular lattice. Parameters are as in Fig. 6. The mass decrease at intermediate U is much smaller than in the case of the square lattice since the intersite bipolarons formed at large U/t are already superlight.
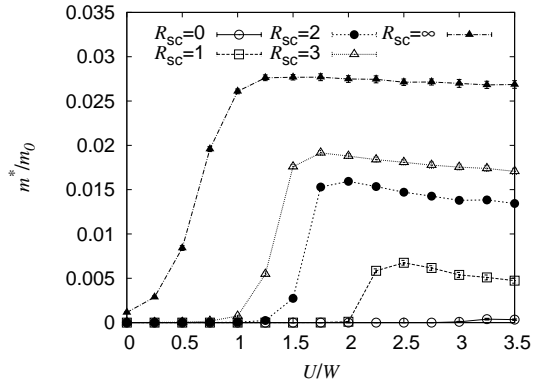

FIG. 9: Comparison of the inverse mass at $\lambda = 1.6$ for bipolarons on the triangular lattice. Parameters are as in Fig. 6.

the bipolaron formed from near-neighbor interactions has slightly more phonons on the square lattice than on the triangular lattice. For the very long range Fröhlich interaction, there are only tiny differences between results for the square and triangular lattices (there are around 2.5% more phonons associated with Fröhlich bipolarons on the triangular lattice). Clearly, the crossover between S0 and S1 bipolarons occurs at approximately the same value of U/W. The strong similarities between the properties of bipolarons on square and triangular lattices on the adiabatic side of the parameter space is quite surprising considering that the properties are very different in the antiadiabatic limit. However, the differences between the bipolarons becomes clearer when the inverse mass is examined.

It has previously been reported that bipolarons on the triangular lattice are small and light[21]. Figure 8 shows the inverse mass of bipolarons on the triangular lattice. Bipolarons formed via the Fröhlich interaction are relatively light, as was observed when the square lattice was considered. The Holstein bipolaron remains qualitatively different to the bipolarons formed with the screened Fröhlich interaction, with an enormous change in the mass of several orders of magnitude over a very small range of U/W as the bipolaron binds. The most significant (and surprising) differences between the bipolarons on square and triangular lattices can be seen when nearest neighbor interactions are considered and when $\lambda = 0.6$ and U is large. For these parameters, the bipolaron on the square lattice is lighter than its counterpart on the triangular lattice (although this does not mean that it is necessarily small). We also note that as λ approaches 1.6, the relative magnitudes of the masses on square and triangular lattices reverses and the bipolaron on the triangular lattice becomes lighter than the bipolaron on the square lattice (the other parameters are held fixed). This is the part of the parameter space where superlight small bipolarons are expected. We will revisit this point when the size of the bipolaron is computed.

Again, a hybrid S0-S1 bipolaron is likely when the S0 and S1 configurations become degenerate. As before, this state is visible as a decrease in the effective mass (increase in inverse effective mass) at intermediate U. A comparison of the inverse masses of bipolarons as interaction range is changed is shown in Fig. 9. There is only a shallow maximum in the inverse mass curve for $R_{sc} = \infty$, but there are more pronounced humps in the curves for smaller values of the screening, corresponding to a light bipolaron. The peaks are not as pronounced for the bipolaron on the triangular lattice as they were when motion
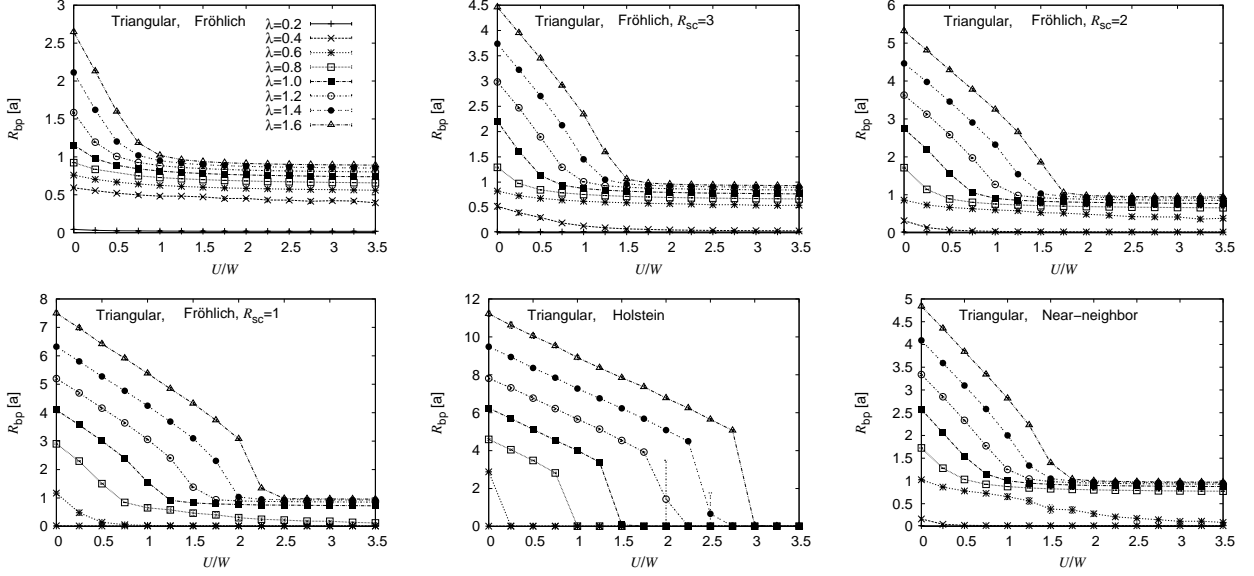
FIG. 10: Inverse size associated with bipolarons on the triangular lattice. Parameters are as in Fig. 6.

was on the square lattice. This is probably because the S1 bipolaron on the triangular lattice at large λ and large U is already light and small with a mass that is 1st order in t[21], so the presence of the hybrid state does not make it significantly easier for the bipolaron to move about on the triangular lattice (whereas on the square lattice, the change from S1 to the hybrid state changes bipolaron hopping processes from 2nd to 1st order in t leading to a reduction in mass).

To finish the examination of the differences between square and triangular lattices, we examine the inverse bipolaron size in figure 10. For large λ, the size of the pair is small and S1 bipolarons are clearly formed in the Fröhlich model at large U (i.e. the radius is approximately one lattice spacing). There are differences between the sizes of bipolarons on triangular and square lattices. Comparison between the radius of the bipolaron on the two lattices shows that the bipolaron on the triangular lattice is significantly smaller than its counterpart on the square lattice at large U. Also, the bipolaron on the triangular lattice is slightly bigger than the pair on the square lattice at very small U. The bipolarons formed on square and triangular lattices have similar size at intermediate U where the pair has hybrid S0-S1 properties. Thus we can see that the slightly larger (but still light) mass of the S1 bipolaron on the triangular lattice is most likely a result of the stronger binding into the S1 state (indeed for large U, the S1 state is very well bound on the triangular lattice at quite small λ - shown by $R_{bp}^{-1} \approx 1$). It is this property of small and light bipolarons that could lead to a bipolaron condensate of S1 bipolarons on a triangular lattice at reasonably high temperatures. However, we have now identified an additional bipolaron configuration which is light and small on both triangular and square lattices, and which is formed at moderate λ and

U: the extra-light hybrid S0-S1 bipolaron.

V. TRIPLETS

We now direct our attention to triplet properties of the bipolaron. The possibility of triplet superconductivity has received a lot of interest since the discovery of spin triplet superconductivity in Sr_2RuO_4[26]. Triplet superconductivity has also been identified in heavy Fermion materials that have a triangular lattice[27]. From the theoretical point of view, triplet pairs could be of interest for two reasons. First, there is a wide literature on BCS to BEC crossover[28,29,30] which is of interest when the parameters governing pairing are intermediate. The presence of stable real-space triplet pairs would add additional limits to this problem, including a crossover or transition between singlet and triplet pairing. Second, the energy difference between singlet and triplet states could be considered as the energy cost of a spin flip, with a direct interpretation as a spin gap[31]. In the next two sections of this article, we discuss the possibility and properties of real space triplet pairs on square and triangular lattices.

A. Hubbard-Holstein model

We start our examination by considering the on-site Hubbard-Holstein interaction. To examine if triplet bipolarons can exist in the 2D Hubbard-Holstein model, we examine the model with very large $U/W = 10$ and compare the energy of two electrons subjected to the Hubbard-Holstein interaction with that of two unbound polarons (Fig. 11). There are several good reasons for
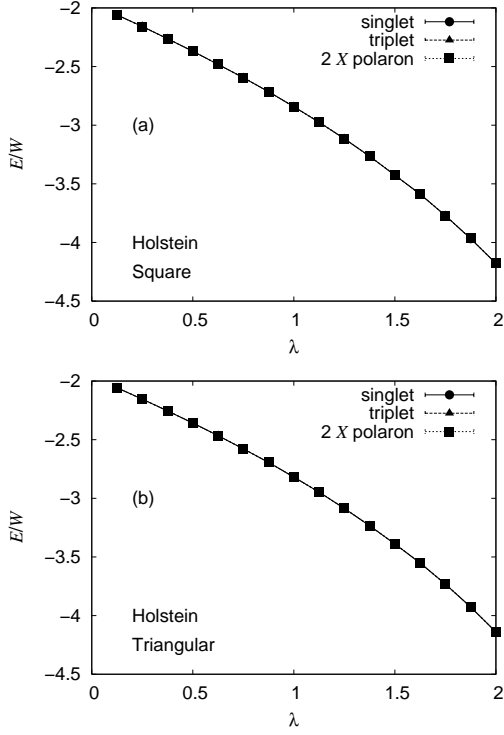
FIG. 11: Absence of triplet bipolaron in the Holstein model on square and triangular lattices. (a) Square lattice, $\bar{\beta} = 7$, $\bar{\omega} = 1$, $U/t = 40$. (b) Triangular lattice, $\bar{\beta} = 14/3$, $\bar{\omega} = 1.5$, $U/t = 60$. Properties are computed at various λ. Note that with the energy expressed in terms of the band-width, lattice type has very little effect on Holstein polarons. The singlet and triplet curves lie under the polaron curve, and are identical to within the statistical error.

doing this. First, as we have seen in the previous sections, the energy of the singlet bipolaron increases monotonically with U, so the binding energy of the singlet bipolaron is minimized, therefore the singlet triplet splitting is also minimized (since triplet states can not have a higher energy than two free polarons without dissociating). Second, since triplet states must have equal or higher energy than singlets, an unbound singlet also implies that the triplet is also not bound. The triplet properties can not depend on U, since a node in the triplet pair wavefunction means that the Hubbard U has no possible effect on triplet properties, so it is sufficient to analyze only this large U limit. We have carefully computed the energies of singlets, triplets and two polarons on triangular and square lattices, and have found no bound triplet states to within the statistical error.

B. Hubbard-Fröhlich model

While there are no triplet bipolarons formed in the Hubbard-Holstein model, the longer range interactions associated with the Hubbard-Fröhlich model can lead directly to inter-site pairing, which is likely to lead to

triplet states. To determine the existence of triplet pairs in the model, we compute the singlet and triplet energies, and compare them with the energy of two polarons, which can be seen in Fig. 12. The parameters associated with the computations are $U = 40t$, $\bar{\beta} = 7$ and $\bar{\omega} = 2$ on the square lattice and $U/t = 60$, $\bar{\omega} = 3$ and $\bar{\beta} = 14/3$ on the triangular lattice. We use the same parameters throughout this section. At weak λ, there are neither singlet nor triplet bound states. On increasing λ, the singlet and triplet states bind at a similar value of λ (the binding can be seen as bifurcations of the curves). At very large λ, the energies of the singlet and triplet become degenerate. This is a result of the interaction on the polaron hopping, which becomes exponentially small. The separation of singlets and triplets in the $U - V$ model on the square lattice scales as t^2, whereas on the triangular lattice the large λ singlet-triplet splitting scales like t. This can be seen in the adiabatic limit as a much larger singlet triplet splitting in the case of the triangular lattice. We note that there are strictly two degenerate triplet states measured here, representing two p-pairings.

The inverse mass of the triplet Fröhlich bipolaron is shown in Fig. 13. At this value of U/W and large electron-phonon coupling, the triplet bipolaron is heavier than the singlet bipolaron, and at weak coupling the triplet is lighter. As U is changed, the triplet properties remain constant, whereas the singlet ones change, notably with an increase in the singlet mass on degrease in U. At very small U, we would expect that the singlet is always heavier. While the strongly coupled singlet bipolaron is clearly lighter on the triangular lattice, which is due to the qualitative effects of lattice type, we do not see any qualitative difference between the mass of the triplets on square and triangular lattices which are very similar.

Figure 14 shows the number of phonons associated with the triplet Fröhlich bipolaron. At strong coupling on the triangular lattice, there is a clear difference between the number of phonons associated with singlet and triplet. In contrast, on the square lattice the number of phonons associated with the two types of bipolaron converges on a single value at large λ. We believe that this is related to the second order hopping on square lattices at strong coupling and first order hopping on triangular lattices. We also note that increasing the electron-phonon interaction range reduces this difference, presumably since the bipolaron has more configurational freedom when R_{sc} is increased, thus allowing similar hopping processes.

Finally, we compute the radius of the triplet Fröhlich bipolaron, which is shown in Fig. 15. There are only small quantitative changes between the radii of triplet bipolarons on different lattices. We note a small finite size effect at weak coupling, which corresponds to a finite inverse radius where the bipolaron is not bound. On increasing λ, the singlet bipolaron is the first to bind strongly, with the triplet radius decreasing slightly, but with the triplet becoming small only for larger λ. In-
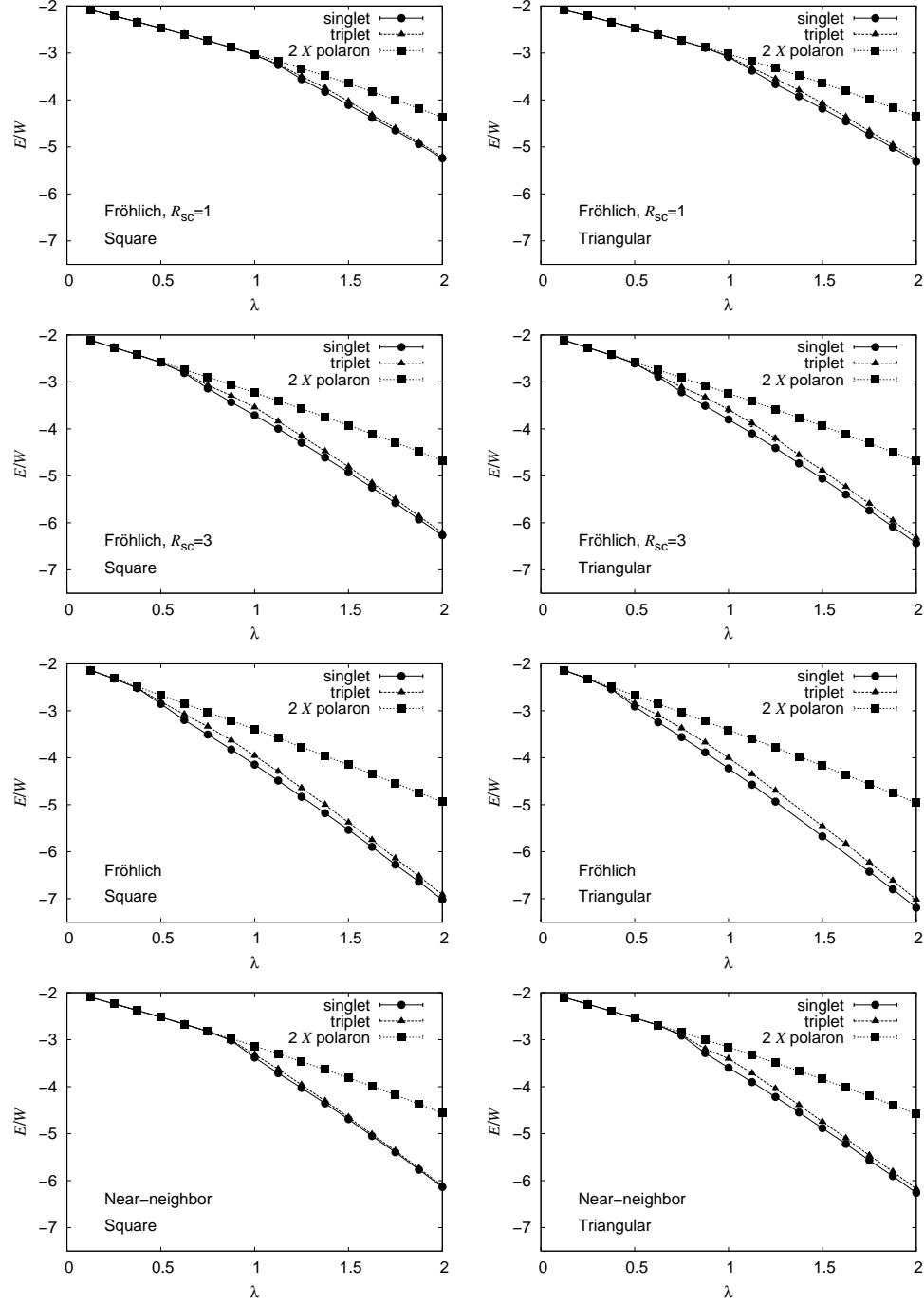
FIG. 12: Total triplet energy of the Fröhlich bipolaron on the square lattice (left) and triangular lattice (right). For the square lattice, $U = 40t$, $\bar{\beta} = 7$, $\bar{\omega} = 2$. On the triangular lattice, $U/t = 60$, $\bar{\omega} = 3$, $\bar{\beta} = 14/3$. λ and the interaction range are varied. For comparison, we also show the singlet energy and the energy of two polarons. As the interaction range increases, the minimum electron-phonon coupling required to bind both singlet and triplet decreases. The singlet energy is very similar on both lattices. However, the singlet-triplet splitting on the triangular lattice is much larger than on the square lattice for all interaction ranges.

creased interaction range decreases the electron-phonon coupling required to bind both types of bipolaron. The strongly bound triplet is slightly larger than the singlet.

VI. DISPERSION

A. Hubbard-Holstein model

To complete our survey of bipolarons in 2D, we consider dispersions of the Hubbard-Holstein and Hubbard-
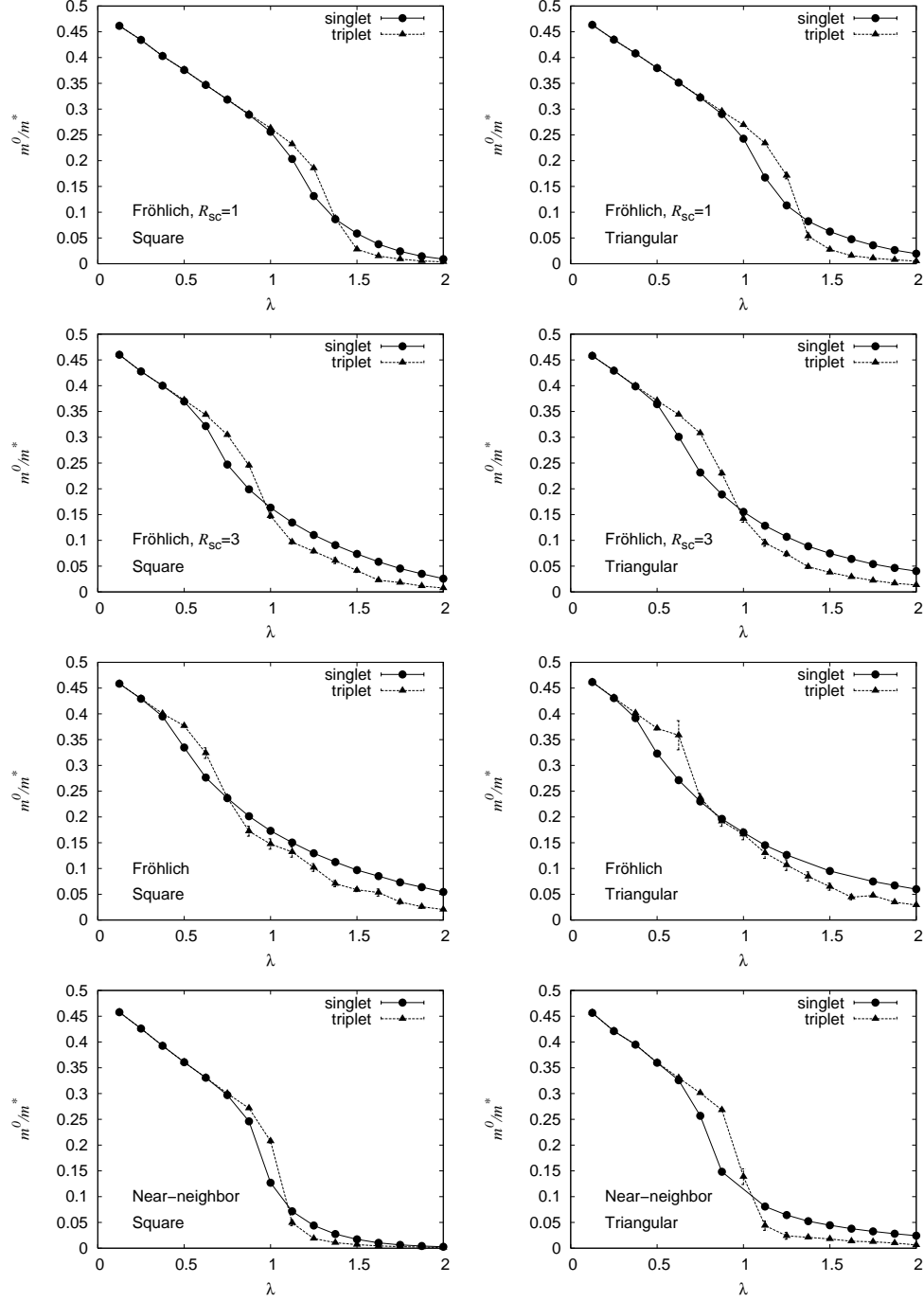
FIG. 13: Inverse mass of the triplet Fröhlich bipolaron. Parameters are as Fig. 12. Error bars represent one standard deviation. At low λ, the triplet bipolaron is lighter than the singlet bipolaron. Note that since properties of the triplet bipolaron do not depend on U, then the singlet will be always be heavier at low U.

Fröhlich bipolarons. The electron-phonon interaction has the potential to lead to unusual effects. For example polaron dispersions in the adiabatic regime of the Holstein model on square and triangular lattices are flattened at the edge of the Brillouin zone[32,33]. It is not known if the dispersion remains flattened once bipolarons form, and also little is known about the dispersions of triplet

bipolarons. Thus, it is of interest to determine how the flat dispersion evolves as a bipolaron is bound from two polarons.

In figure 16 we show singlet dispersions of the Hubbard-Holstein bipolaron on the square lattice when $\lambda = 1.45$ and $\bar{\omega} = 1$. Computation of the dispersion is carried out using the same method as in Ref. 16. At large
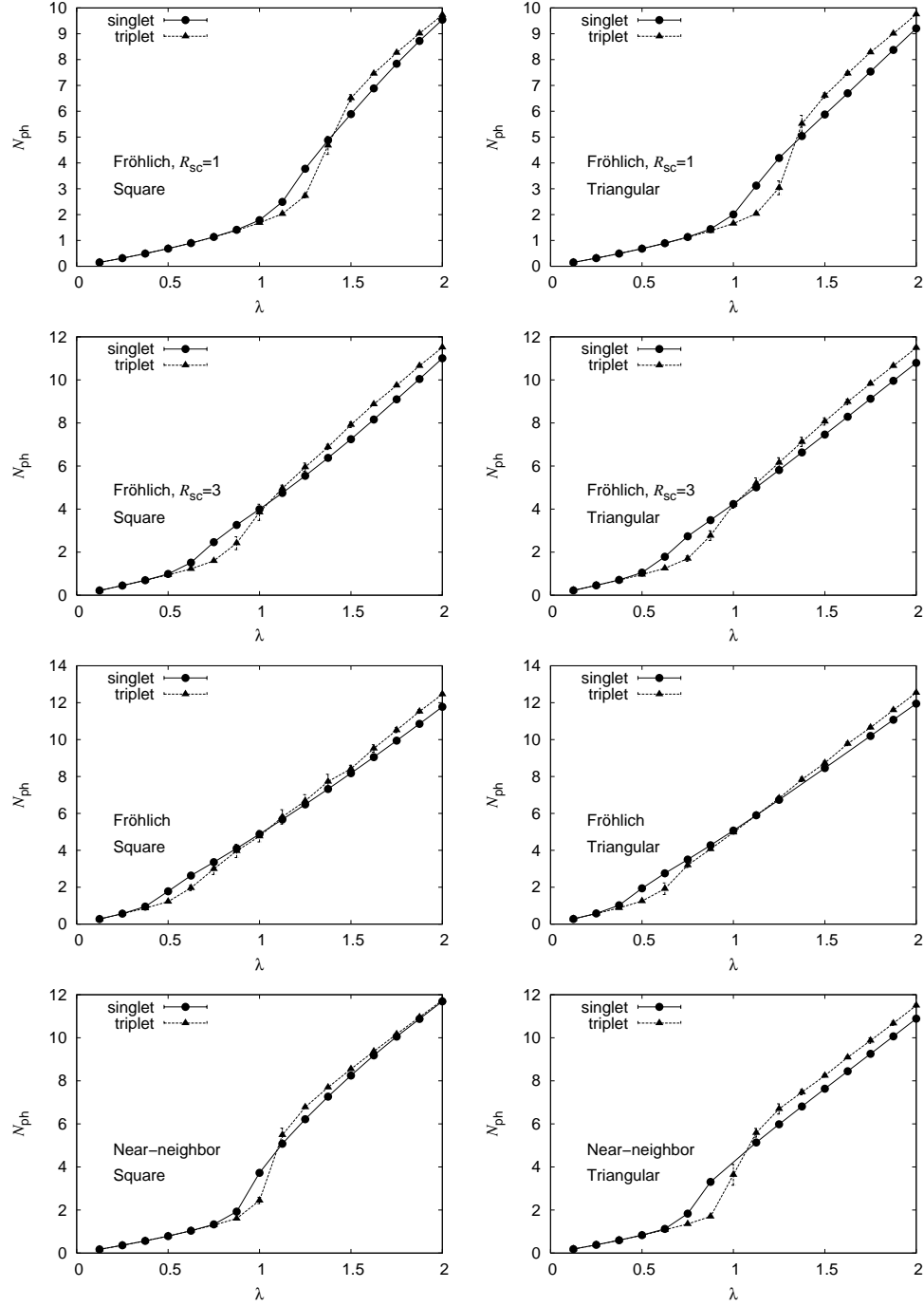
FIG. 14: Number of phonons associated with the triplet Fröhlich bipolaron. Parameters are as Fig. 12.

U, the bipolaron is unbound and the dispersion represents two polarons. The dispersions relating to $U/t = 12$, $U/t = 11.6$ and $U/t = 11.2$ are indistinguishable to the eye (top panel). As the repulsion is decreased, there is a decrease in bandwidth of several orders of magnitude at the U corresponding to the binding of the bipolaron. In the lower panel, we also show dispersions normalized by $\epsilon_M - \epsilon_0$ (ϵ_M is the energy of the bipolaron at the M point) so that the forms of the dispersion function can be compared to the non-interacting tight-binding dispersion. At large U, the form of the dispersion of the two polarons (and the weakly bound bipolaron) is quite distorted away from the form of the tight-binding dispersion. As U decreases further, the electrons become tightly bound into an on-site bipolaron. Then the form of the dispersion tends towards that of the tight-binding spectrum. We believe this to be the effect of the strongly bound bipolaron acting as a single particle, with a new hopping in-
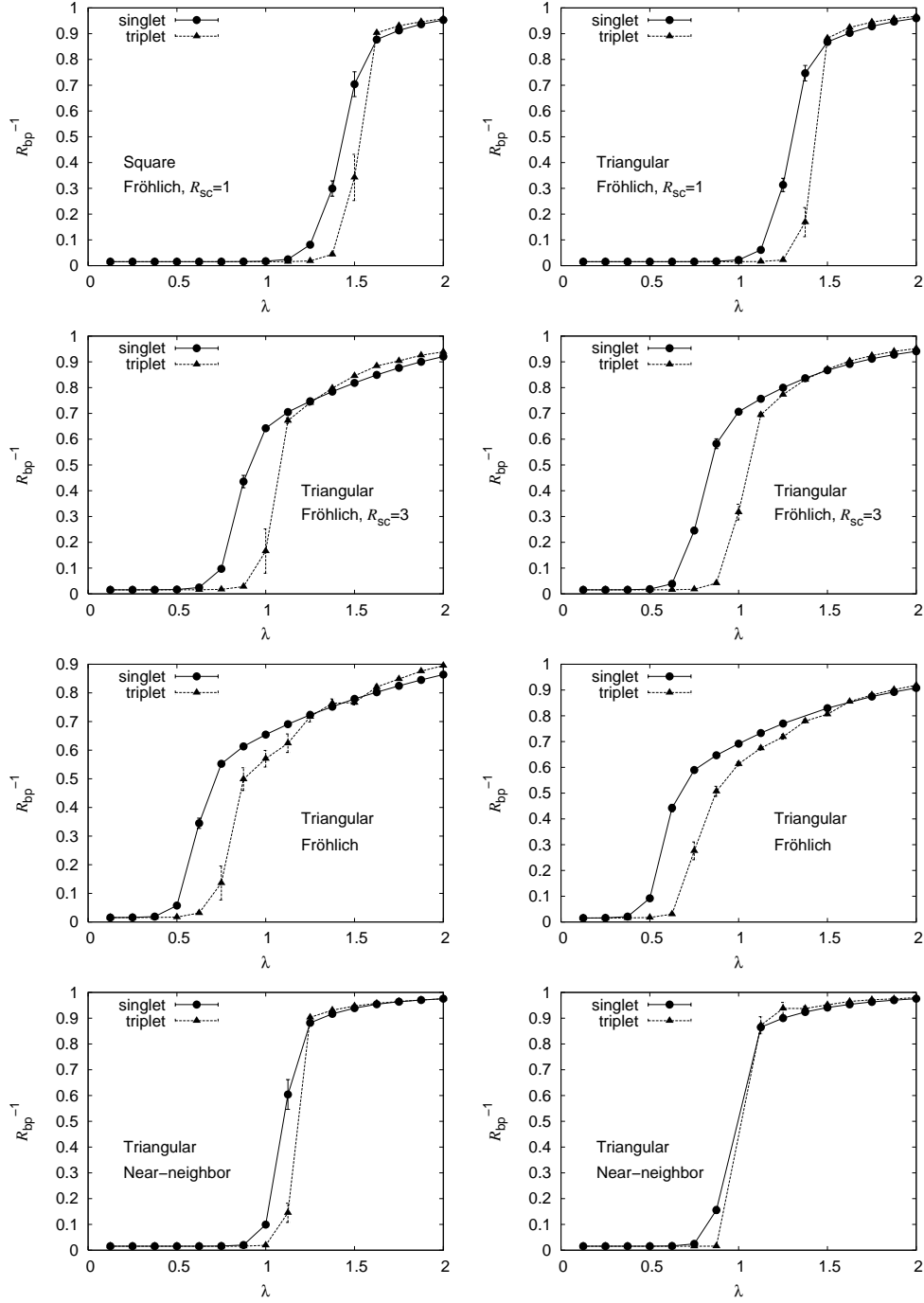
FIG. 15: Radius of the Fröhlich triplet bipolaron. Parameters are as Fig. 12.

tegral that relates to the overlap of the wavefunction of the pair between sites.

In figure 17 we show the variation of the singlet dispersions of the Hubbard-Holstein bipolaron on the triangular lattice when $\lambda = 1.45$, $\bar{\omega} = 1.5$ and U is varied. Again, the functional form of the spectrum tends towards the tight-binding dispersion as pairs become strongly bound, although it becomes increasingly difficult to collect data since the fractional variance on the dispersion increases as

λ increases. Again, we suggest that the similarity in functional forms is due to the tightly bound bipolaron acting as a single particle with a single (albeit small) inter-site hopping parameter. For the Holstein bipolaron, the pair wavefunction is small, and the lattice distortion is highly localized.
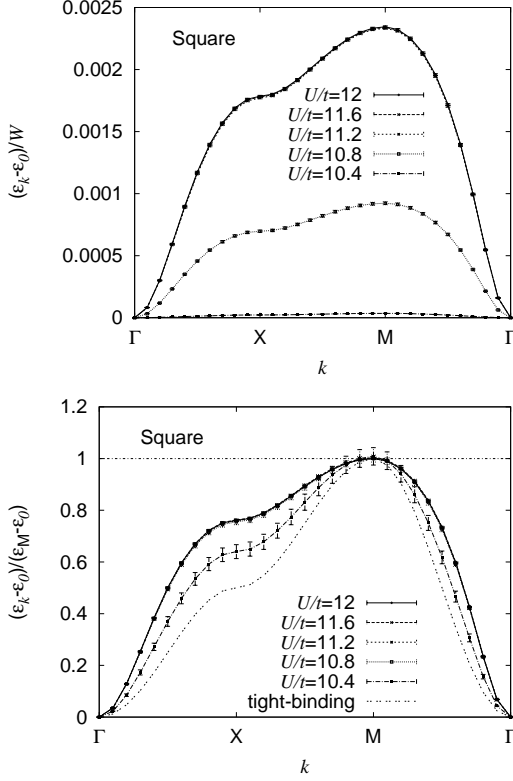
FIG. 16: Singlet dispersions of the Hubbard-Holstein bipolaron on the square lattice when $\lambda = 1.45$, $\bar{\beta} = 14$ and $\bar{\omega} = 1$. U is varied. Note that error bars on the plots of dispersions represent one standard deviation. The lower panel shows the dispersions normalized by $\epsilon_{\mathrm{M}} - \epsilon_0$ compared to the normalized tight binding dispersion. As U decreases, the bipolaron becomes strongly bound on-site and the dispersion develops a form closer to the tight-binding approximation.

FIG. 17: Singlet dispersions of the Hubbard-Holstein bipolaron on the triangular lattice when $\lambda = 1.45$, $\bar{\beta} = 28/3$ and $\bar{\omega} = 1.5$. U is varied. Error bars represent one standard error. There is a very rapid change in the bandwidth between $U/t = 15.6$ and $U/t = 16.8$. This coincides with a change in the shape of the dispersion from the flattened to the tight binding form.

B. Hubbard-Fröhlich model

We also examine the dispersions of the Hubbard-Fröhlich model. In Fig. 18, we show the dispersion for the square lattice when the Fröhlich interaction with $R_{sc} = 2$ is considered. The panels show the effects of changing U. At large U, the bipolaron is bound into an intersite (S1) configuration. There are two main features that should be emphasized. The first is remarkable. As the Coulomb repulsion decreases, the bandwidth *increases* significantly, i.e. although the bipolaron becomes more strongly bound, it becomes lighter. This is the same effect as seen in section III, where the mass was shown to decrease at intermediate U as a new type of hybrid S0-S1 crab bipolaron forms. At small U, the degeneracy of the S0 and S1 bipolarons is broken and the bandwidth decreases with U.

The second feature in Fig. 18 is that the shape of the bipolaron dispersion changes dramatically as it it bound onsite. For large U, the dispersion is flattened, whereas for the strongly bound onsite pair ($U/t = 5$) the d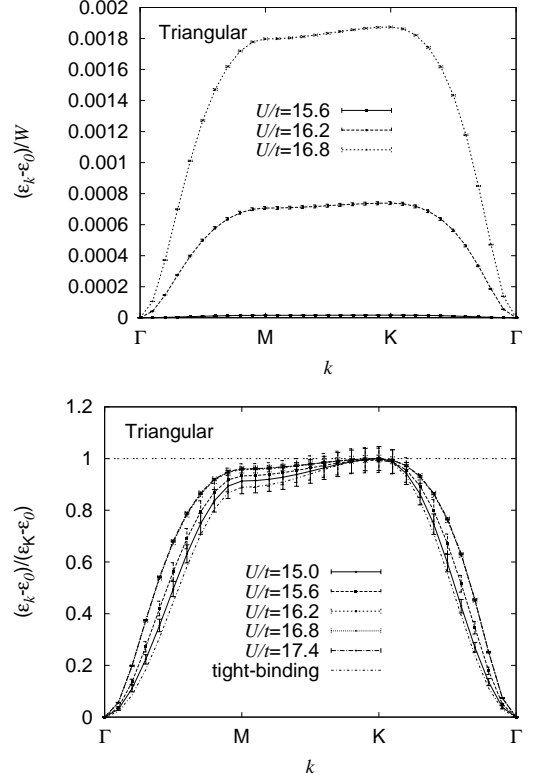ispersion has the characteristic tight-binding shape (albeit strongly renormalized by interactions). We consider this effect to relate to the change between hopping mechanisms. For a weakly bound bipolaron, the wavefunction is large and single polaron-like hops dominate the motion of the particle, whereas for the strongly bound bipolaron, the pair wavefunction is smaller than a single lattice site and a new hopping integral becomes relevant, which is relating to the tunneling of the whole bipolaron between sites. The dispersions of triplet states on the square lattice are also shown in the panel relating to $U/t = 40$. The triplet state is higher in energy and has a narrower bandwidth. Singlet and triplet dispersions do not cross.

We also examine the dispersions of the Coulomb-Fröhlich bipolaron on a triangular lattice, which are shown in Fig. 19. The first significant difference between bipolarons on square and triangular lattices is the existence of superlight bipolarons at large $U \to \infty$. These contribute to a factor of ~ 4 difference between the bandwidths of the bipolaron on square and triangular lattices. Again, as U decreases there is a remarkable increase in the bandwidth. This effect is not as dramatic as in the case of the square lattice, presumably because the bipolaron already moves with a crab like motion at
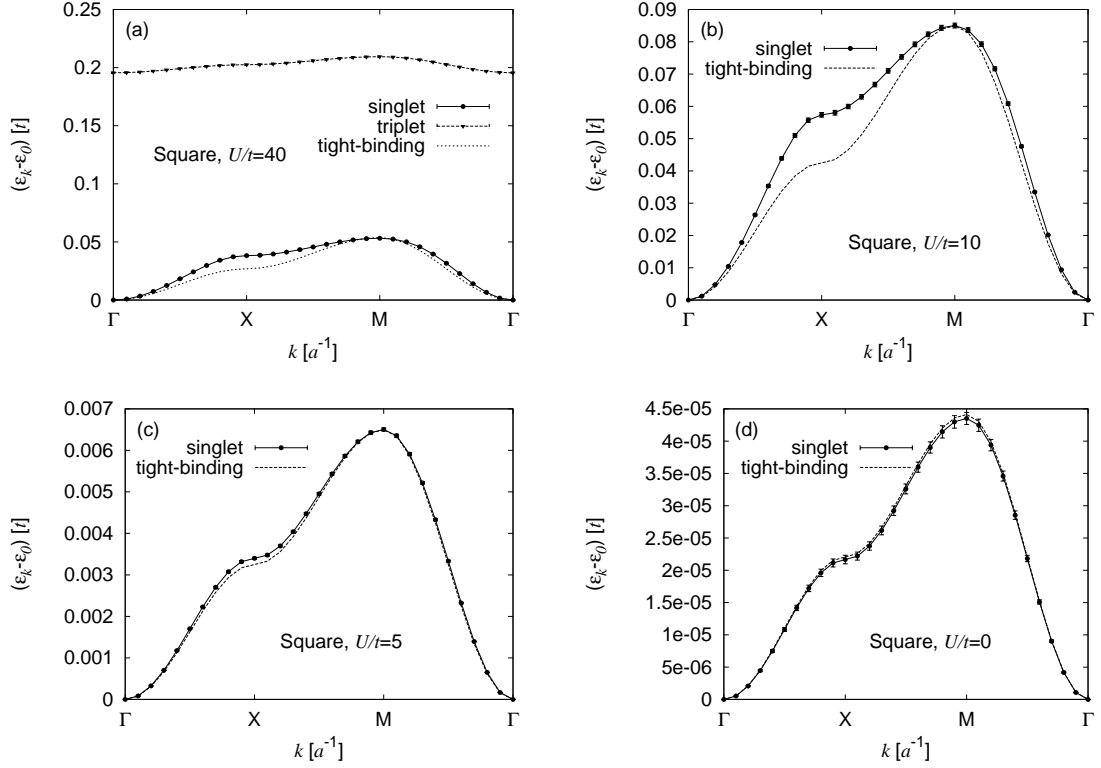
FIG. 18: Singlet dispersions of the Hubbard-Fröhlich model on the square lattice. The triplet dispersion is shown in panel (a). For comparison, the tight-binding dispersion normalized to the bandwidth is also shown. $\lambda = 1.45$, $\bar{\omega} = 1$, $R_{sc} = 2$ and $\bar{\beta} = 14$. Error bars show one standard deviation. As U decreases and the bipolaron becomes strongly bound onsite, the shape of the dispersion becomes consistent with that of a tightly-bound particle. An increase in the band-width can be seen initially on decreasing U corresponding to the formation of the hybrid S0-S1 bipolaron. For smaller U, the S0 bipolaron is tightly bound and the dispersion is narrow.

large U. However the degeneracy between $S0$ and $S1$ bipolarons accounts for an additional $\sim 20\%$ increase in the bandwidth, making the bipolarons extra-light. This shows how bipolarons can be light over an extremely large regime of the parameter space on triangular lattices.

To highlight the effect of the formation of the hybrid S0-S1 bipolaron on the dispersion, Fig. 20 shows a comparison of the variation of the bandwidth as U is changed. The bandwidths of bipolarons on both square and triangular lattices are shown, although it should be noted that the scales are different. There is an increase in bandwidth at $U/W \sim 3$. The widening of the bandwidth is more significant for the square lattice, but is also visible for the triangular lattice. The broadening of the bandwidth on the square lattice at intermediate to large U is important, since it shows that light bipolarons are not confined to lattices constructed from triangular plaquettes, but can also exist on simple square, linear and presumably cubic lattices.

As noted in the introduction, we can also consider the properties of bipolarons formed from a simplified nearest-neighbor interaction as a means to compare with analytical results. Fig. 21 shows the variation of the singlet and triplet dispersions in the near-neighbor model as ω is

changed . Bipolarons are considered on both square and triangular lattices with a large electron-phonon coupling of $\lambda = 8$. To make comparisons with the UV-model, we choose a large phonon frequency $\omega = 120t$ on the triangular lattice (and $\omega = 80t$ on the square lattice). A large coulomb repulsion of $U = 120t$ ($U = 80t$) stops on-site pairing, which leads to a $U - V$ model with $\tilde{U} = 24t$ ($\tilde{U} = 16t$) and $\tilde{V} = 48t$ ($\tilde{V} = 32t$). We also compute the dispersions of bipolarons on the triangular lattice when $\bar{\omega} = 30$ and $\bar{\omega} = 6$ ($\bar{\omega} = 20$ and $\bar{\omega} = 4$ on the square lattice).

The dispersion of the near-neighbor bipolaron on the triangular lattice at large phonon frequency yields an unusual result. The singlet and triplet bands cross. We note again that the QMC algorithm picks out only the lowest energies associated with singlet and triplet states. In the plot, the s band is visible, along with the lowest p band. A crossing is very unexpected, since in all situations that we have previously studied, the triplet band has always sat above the singlet one. This indicates that there will be a transition from singlet to triplet states if sufficient momentum can be imparted to the bipolarons. The crossing remains down to lower phonon frequencies $\hbar\omega \sim 5W$, but is not visible in the adiabatic regime.
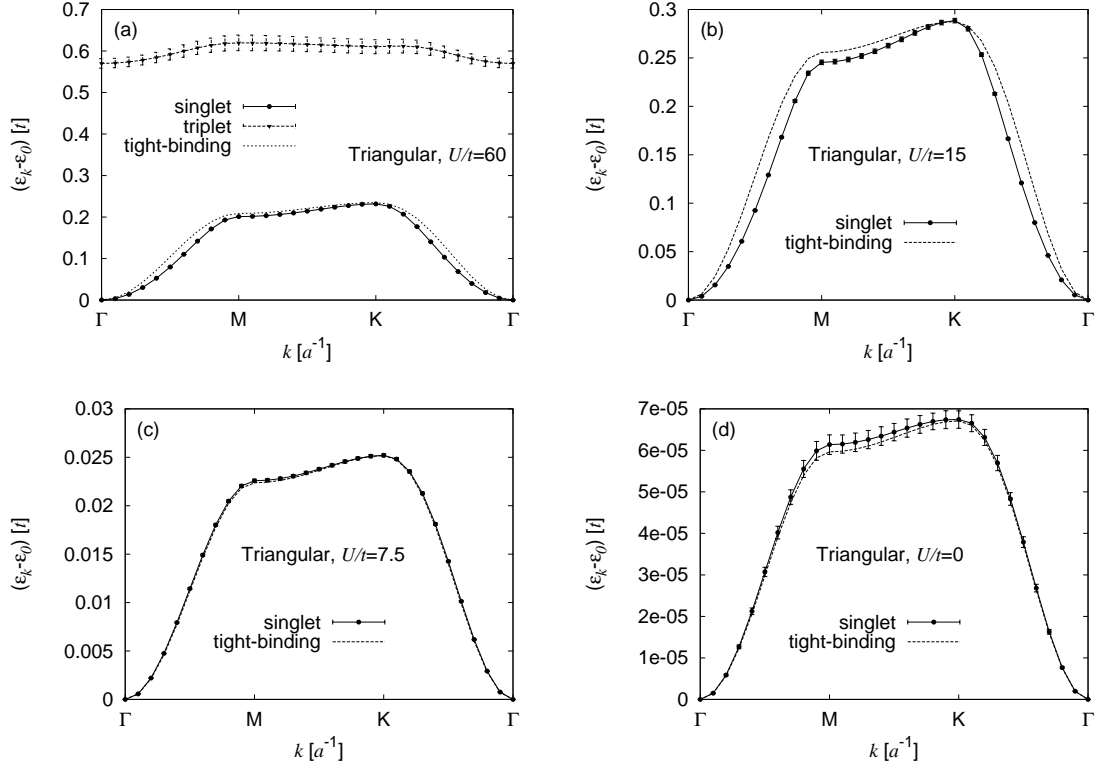
FIG. 19: Singlet dispersions of the bipolaron formed in the screened Hubbard-Fröhlich model on the triangular lattice. $R_{sc} = 2$, $\lambda = 1.45$, $\bar{\omega} = 1.5$, $\bar{\beta} = 28/3$ and U is varied. Error bars represent one standard deviation. As U is decreased, the bandwidth initially *increases* as the S0-S1 hybrid bipolaron is approached from the S1 bipolaron (until around $U/t = 15$). For small U, the S0 bipolaron is approached, and the bandwidth decreases significantly. For reference the tight-binding dispersion normalized to the same bandwidth is also plotted. The triplet dispersion is shown in panel (a).
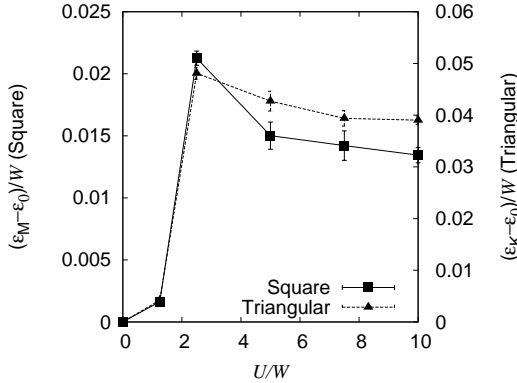

FIG. 20: Comparison of the variation of the bandwidth with U for the square and triangular lattices. The widening of the bandwidth at intermediate U is more significant for the square lattice, but is also visible for the triangular lattice.

In the appendix, we summarize the analytical approach to solving the UV-model on a triangular lattice when pairs have finite momentum, and the full dispersion can be seen in Fig. 22. The energy level crossing is clearly visible, and by comparison it is clear that a single s band

and a single p band are visible in Fig. 21. Note that there are are a total of 6 possible bands associated with the bipolaron, although it is unlikely that the higher energy bands would be excited in any normal transport process.

The band crossing can not be seen for bipolarons on the square lattice, rather the singlet and triplet pairs become degenerate at the zone edge as the phonon frequency increases. This feature is also visible in the dispersion of bipolarons on the chain[16], and is probably a generic feature of bipolarons on lattices with cubic symmetry.

VII. SUMMARY

In this paper, we computed the properties of bipolarons on two-dimensional lattices using a continuous time quantum Monte Carlo algorithm. Properties of the bipolaron including the total energy, inverse mass, bipolaron radius and number of phonons associated with the bipolaron demonstrated the qualitative difference between models of electron phonon interaction with long-range interaction (screened Fröhlich) and those with purely local (Holstein) interaction, with only small long range tails needed to completely change the properties of the bipolaron. A major result of our survey of the pa-
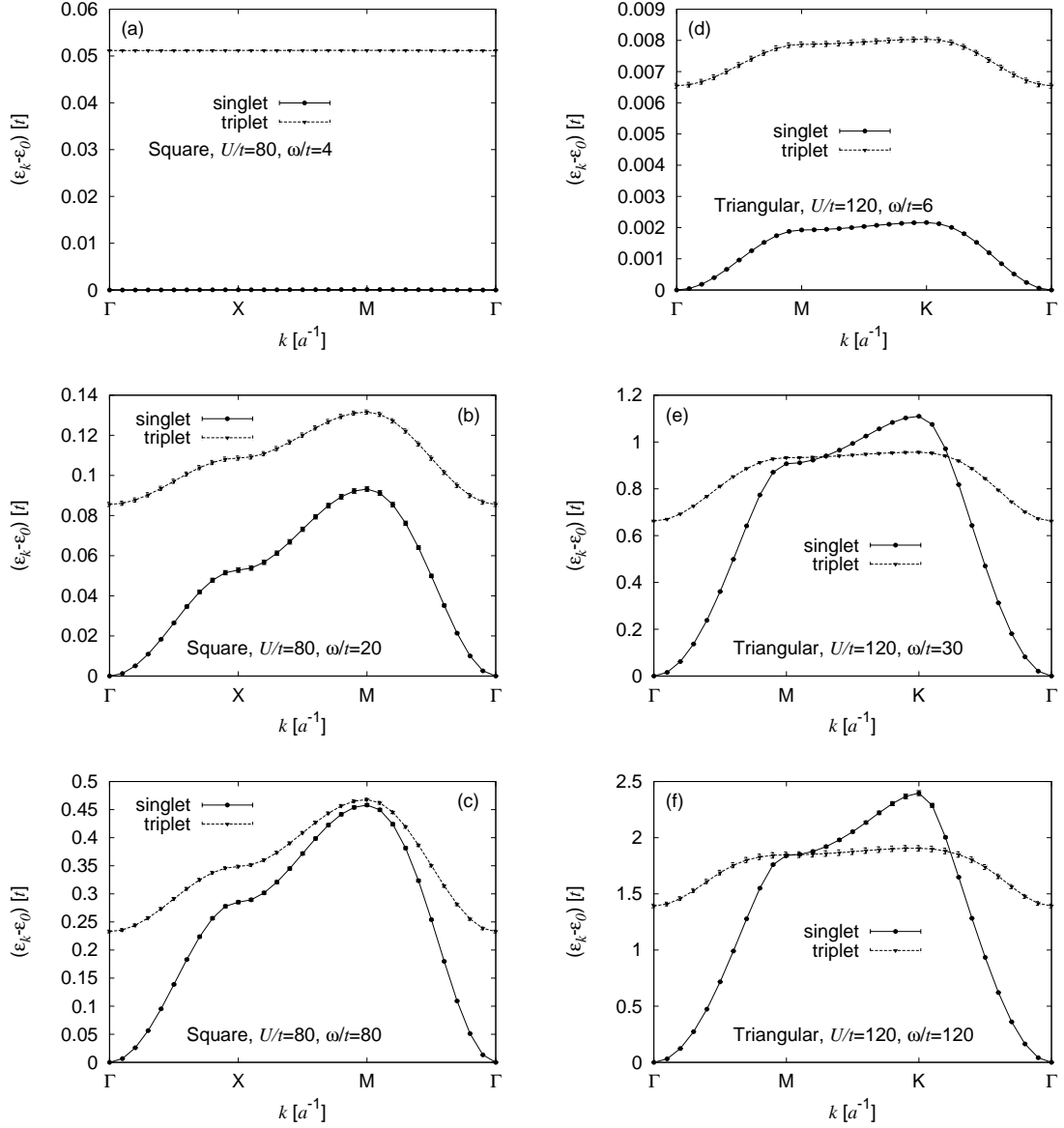
FIG. 21: Graphs showing the variation of the singlet and triplet dispersions in the near-neighbor model with ω with $\lambda = 8$, $\omega = 120t$ ($\omega = 80t$), $U = 120t$ ($U = 80t$) to match with a $U - V$ model with $\bar{U} = 24t$ ($\bar{U} = 16t$) and $\bar{V} = 48t$ ($\bar{V} = 32t$). Also $\bar{\omega} = 30$ and $\bar{\omega} = 6$ (and equivalent for the square lattice, $\bar{\omega} = 20$ and $\bar{\omega} = 4$).

rameter space is the existence of extra-light hybrid bipolarons consisting of an on-site and an off-site component when on-site and inter-site bipolaron configurations are degenerate, similar to the previously reported superlight bipolarons, but slightly lighter on the triangular lattice, and significantly lighter than the intersite bipolarons on the square lattice. We also compute triplet properties of the bipolarons. A major surprise is that triplet pairs with large momentum (close to the K point) are more stable than singlet states on the triangular lattice.

The potential for the existence of local triplet pairs that are preferentially bound has the potential to open new avenues in the theory of superconductivity. At low momenta, triplet pairs are necessarily higher in energy than their singlet counterparts since an exact theorem requires the ground state wavefunction of a pair to have no nodes. No such theorem exists for states with high pair momentum, however the existence of stable triplet states is unexpected. Thus, in addition to the potential for BCS-BEC crossover as the attractive potential is tuned, there is an additional possibility of triplet BCS to triplet BEC crossover, or even a transition between singlet and triplet pairing. We believe that such a possibility should be investigated further.

Our other finding of light hybrid bipolarons on the square lattice at intermediate coupling and Coulomb re-

pulsion is also significant. While the effect only exists over a very narrow range of coupling constants, it shows that exotic lattice types are not necessary for small light pairs that could have potential to form a high temperature Bose condensate. As in the case of the triangular lattice, light pairs are only a prerequisite for a high temperature BEC, as other factors such as an absence of clustering need to be confirmed. Work to discuss this clustering will form the basis of a future publication, but clearly there are still some surprises left in the bipolaron problem.

VIII. ACKNOWLEDGEMENTS

APPENDIX A: UV MODEL ON THE TRIANGULAR LATTICE

The quantum-mechanical problem of two interacting particles on a lattice can be solved exactly as long as the radius of the interaction is finite. Of special interest here is the spectrum of bound pairs that form when at least part of the potential is attractive. The general solution of the bound state problem results in a spectral equation[34,35,36] in the form of a determinant with a size equal to the number of lattice sites within the interaction range. For the non-retarded UV model with on-site Hubbard repulsion U and nearest-neighbor attraction $-V$, the determinant is 3×3 for the one-dimensional chain, 5×5 for the square lattice, 7×7 for the triangular lattice, and so on. The subsequent analysis can be simplified by considering the symmetric and anti-symmetric states (that is the singlets and triplets) separately. This effectively halves the number of interaction sites, and halves the size of the determinants as a result. For the UV-model on the triangular lattice, the size of the singlet determinant reduces to 4 (symmetric combinations of the nearest neighbors plus the central site), and that of the triplet determinant to 3 (anti-symmetric combinations of the nearest neighbors).

Omitting the straightforward but lengthy derivation, the spectral equation for the singlet bound pair of the lattice momentum $\boldsymbol{K}$ is

$$\begin{vmatrix} US_{00}-1 & -VS_{01} & -VS_{02} & -VS_{03} \\ -VS_{10} & -VS_{11}-1 & -VS_{12} & -VS_{13} \\ -VS_{20} & -VS_{21} & -VS_{22}-1 & -VS_{23} \\ -VS_{30} & -VS_{31} & -VS_{32} & -VS_{33}-1 \end{vmatrix} = 0 ,$$

(A1)

where

$$S_{j0}(\boldsymbol{K}) = \frac{1}{N} \sum_{\boldsymbol{q}} \frac{e^{i\boldsymbol{q}\boldsymbol{n}_j}}{E + \Delta(\boldsymbol{K}, \boldsymbol{q})} ,$$
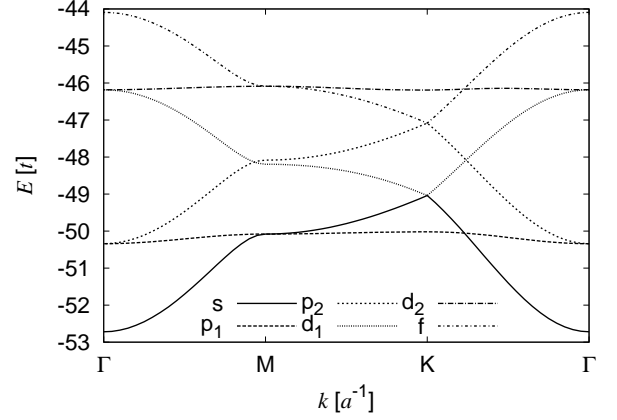
(A2)

FIG. 22: The spectrum of bound pair in the UV model on the triangular lattice. $U = 24\,t$ and $V = 48\,t$, which corresponds to $\lambda = 8$, $U = 20W$ and $\omega \to \infty$. Notice the crossing of the lowest singlet and triplet states near the edge of the Brillouin zone at the M point.

$$S_{jk}(\boldsymbol{K}) = \frac{2}{N} \sum_{\boldsymbol{q}} \frac{e^{i\boldsymbol{q}\boldsymbol{n}_j} \cos(\boldsymbol{q}\boldsymbol{n}_k)}{E + \Delta(\boldsymbol{K}, \boldsymbol{q})} ,$$

(A3)

$$\begin{aligned} \Delta(\boldsymbol{K}, \boldsymbol{q}) =\ & 4t \cos\frac{K_x}{2} \cos q_x \\ & + 8t \cos\frac{K_x}{4} \cos\frac{\sqrt{3}K_y}{4} \cos\frac{q_x}{2} \cos\frac{\sqrt{3}q_y}{2} \\ & + 8t \sin\frac{K_x}{4} \sin\frac{\sqrt{3}K_y}{4} \sin\frac{q_x}{2} \sin\frac{\sqrt{3}q_y}{2} .\end{aligned}$$ (A4)

Here the vectors $\boldsymbol{n}_{j,k}$ denote the nearest neighbor sites of the triangular lattice: $\boldsymbol{n}_0 = (0,0)$; $\boldsymbol{n}_1 = (1,0)$; $\boldsymbol{n}_2 = (\frac{1}{2}, \frac{\sqrt{3}}{2})$; $\boldsymbol{n}_3 = (-\frac{1}{2}, \frac{\sqrt{3}}{2})$.

The equation (A1) can be solved numerically with respect to the pair energy E for the given pair momentum $\boldsymbol{K}$. For a positive on-site repulsion U and a large enough intersite attraction V, the equation has three roots that we denote s, d_1 and d_2 states. The evolution of the energies as a function of $\boldsymbol{K}$ is shown in figure 22 At the high-symmetry points of the Brillouin zone, the system of equations (A1) can be further diagonalized into smaller blocks by a proper linear transformation. Thus, at the Γ point $\boldsymbol{K} = (0,0)$, the spectrum splits into the standalone ground state s and a degenerate doublet (d_1, d_2). In the corner of the Brillouin zone, the states s and d_1 become degenerate, as can be seen from figure 22.

The triplet bound states can be treated similarly. The exact spectrum equation is a 3×3 determinant:

$$\begin{vmatrix} -VT_{11}-1 & -VT_{12} & -VT_{13} \\ -VT_{21} & -VT_{22}-1 & -VT_{23} \\ -VT_{31} & -VT_{32} & -VT_{33}-1 \end{vmatrix} = 0 ,$$

(A5)

$$T_{jk}(\boldsymbol{K}) = \frac{(-2i)}{N} \sum_{\boldsymbol{q}} \frac{e^{i\boldsymbol{q}\boldsymbol{n}_j} \sin(\boldsymbol{q}\boldsymbol{n}_k)}{E + \Delta(\boldsymbol{K}, \boldsymbol{q})} ,$$

(A6)

with the same meaning of $\boldsymbol{n}_{j,k}$ and Δ. The equation does not depend on the on-site repulsion at all, as expected. At the Γ point, the spectrum splits into a low-energy doublet (p_1, p_2), and a standalone high-energy f-state, (see figure 22). At the K-point, p_2 and f are degenerate.

Two comments are in order. (i) For strongly-coupled pairs, the classification of the different orbital states is basically the one of a single particle on a six-site tight-binding ring. (ii) Notice the general property of level crossing between the lowest singlet and triplet states. While the singlet is always the ground state at small momenta, the triplet becomes the lowest state at large momenta. The same property has been observed for the bipolaron, as discussed in the main text of the paper.

[1] J.G.Bednorz and K.A.Müller, Z. Phys. B **64**, 189 (1986).

[2] Y. Kamihara, T. Watanabe, M. Hirano, and H. Hosono, J. Am. Chem. Soc. **130**, 3296 (2008).

[3] K. Takada, H. Sakurai, E. Takayama-Muromachi, F. Izumi, R. A. Dilanian, and T. Sasaki, Nature **422**, 53 (2003).

[4] P. Anderson, *The Theory of Superconductivity in the Cuprates* (Princeton University Press, Princeton, NY, 1997).

[5] P. Monthoux, A. V. Balatsky, and D. Pines, Phys. Rev. B **46**, 14803 (1998).

[6] R. B. Laughlin, Philosophical Magazine **86**, 1165 (2006).

[7] A. S. Alexandrov, *Theory of Superconductivity: From Weak to Strong Coupling* (IOP, Bristol, 2003).

[8] T. M. Hardy, J. P. Hague, J. H. Samson, and A. S. Alexandrov, Phys. Rev. B **79**, 212501 (2009).

[9] J. M. Tranquada, B. J. Sternlieb, J. D. Axe, Y. Nakamura, and S. Uchida, Nature **375**, 561 (1995).

[10] A. S. Mishchenko and N. Nagaosa, Phys. Rev. B **73**, 092502 (2006).

[11] J. P. Carbotte, E. Schachinger, and D. N. Basov, Nature **401**, 354 (1999).

[12] G. Wellein, H. Röder, and H. Fehske, Phys. Rev. B **53**, 9666 (1996).

[13] A. Weiße, H. Fehske, G. Wellein, and A. R. Bishop, Phys. Rev. B **62**, R747 (2000).

[14] J. Bonča, T. Katrašnik, and S. A. Trugman, Phys. Rev. Lett. **84**, 3153 (2000).

[15] E. Jeckelmann, C. Zhang, and S. R. White, Phys. Rev. B **60**, 7950 (1999).

[16] J. P. Hague and P. E. Kornilovitch, Phys. Rev. B **80**, 054301 (2009).

[17] M. Hohenadler, M. Aichhorn, and W. von der Linden, Phys. Rev. B **71**, 014302 (2005).

[18] M. Hohenadler and W. von der Linden, Phys. Rev. B **71**, 184309 (2005).

[19] A. S. Alexandrov, Phys. Rev. B **53**, 2863 (1996).

[20] A. S. Alexandrov and P. E. Kornilovitch, J. Phys.: Condens. Matter **14**, 5337 (2002).

[21] J. P. Hague, P. E. Kornilovitch, J. H. Samson, and A. S. Alexandrov, Phys. Rev. Lett. **98**, 037002 (2007).

[22] J. P. Hague, P. E. Kornilovitch, J. H. Samson, and A. S. Alexandrov, J. Phys.: Condens. Matter **19**, 255214 (2007).

[23] A. Macridin, G. A. Sawatzky, and M. Jarrell, Phys. Rev. B **69**, 245111 (2004).

[24] J. Bonča and S. A. Trugman, Physica C **364-365**, 141 (2001).

[25] J. Bonča and S. A. Trugman, Journal of Superconductivity: Incorporating Novel Magnetism **13**, 999 (2000).

[26] K. Ishida, H. Mukuda, Y. Kitaoka, K. Asayama, Z. Q. Mao, Y. Mori, and Y. Maeno, Nature **396**, 658 (1998).

[27] K. Ishida, D. Ozaki, T. Kamatsuka, H. Tou, M. Kyogaku, Y. Kitaoka, N. Tateiwa, N. K. Sato, N. Aso, C. Geibel, et al., Phys. Rev. Lett. **89**, 037002 (2002).

[28] R.Micnas, J.Ranninger, and S.Robaszkiewicz, Rev. Mod. Phys **62**, 113 (1990).

[29] P. Nozieres and S. Schmitt-Rink, J. Low Temp. Phys. **59**, 95 (1985).

[30] M. Randeria, N. Trivedi, A. Moreo, and R. T. Scalettar, Phys. Rev. Lett. **69**, 2001 (1992).

[31] A. S. Alexandrov and N. Mott, *High temperature superconductors and other superfluids* (Taylor and Francis, London, 1994).

[32] P. E. Kornilovitch, Phys. Rev. Lett. **81**, 5382 (1998).

[33] J. P. Hague, Phys. Rev. B **73**, 060503(R) (2006).

[34] P. E. Kornilovitch, *Polarons and Bipolarons in High-Tc Superconductors and Related Materials* (Cambridge University Press, 1995), chap. 23, p. 367.

[35] P.E.Kornilovitch, Ph.D. thesis, King's College London (1997).

[36] P. E. Kornilovitch, Phys. Rev. B **69**, 235110 (2004).

[37] The strict analogue of the near-neighbor model would have ions above near-neighbor bonds, which would only interact with electrons at the ends of those bonds. In that case, $\Phi(\boldsymbol{a}) = \Phi(0)/4$ for the square lattice and $\Phi(\boldsymbol{a}) = \Phi(0)/6$ on the triangular lattice.